JOINT EUROPEAN TORUS

JET–P(92)63

J.W. Connor, G.P. Maddison, H.R. Wilson, G. Corrigan,
T.E. Stringer, F. Tibone and JET Team

An Assessment of Theoretical Models Based on Observations in the JET Tokamak Part I: Ion Heat Transport due to VTi Instabilities

An Assessment of Theoretical Models Based on Observations in the JET Tokamak Part I: Ion Heat Transport due to VTi Instabilities

J.W. Connor[1], G.P. Maddison[1], H.R. Wilson[1], G. Corrigan,
T.E. Stringer, F. Tibone and JET Team*

JET-Joint Undertaking, Culham Science Centre, OX14 3DB, Abingdon, UK

[1]AEA Fusion, Culham Laboratory (UKAEA/Euraton Fusion Association) Abingdon, Oxon, OX14 3DB
** See Annex*

Preprint of Paper to be submitted for publication in
Plasma Physics and Controlled Fusion

1. *Introduction*

The plasma physics literature abounds with theoretical expressions for anomalous transport coefficients (see the earlier review by Liewer [1]) purporting to explain the confinement properties of tokamaks, often on the basis of crude comparisons at the level of energy confinement time scalings. The availability of spatially resolved measurements of most plasma parameters in present-day tokamaks allows a more detailed and stringent assessment of theoretical transport models, based on comparisons with local heat fluxes and transport coefficients inferred from the experimental data.

Such an approach has been followed at JET for several years. Initial results presented in [2] had highlighted the inability of models based on drift wave instabilities to describe the observed local heat fluxes in representative plasma conditions. Similar conclusions emerged from a subsequent more extensive analysis of the energy transport properties of the plasma ions [3].

In the intervening years experimental information of increasing quality has accumulated in JET, covering a wider range of plasma parameters and regimes. At the same time, several new theoretical developments have been proposed. Thus it is now possible to undertake a more comprehensive comparison between theory and experiment on an unprecedented statistical basis.

The present paper focuses on anomalous ion energy transport. A survey of the relevant literature has been carried out and published transport coefficients have been collected together, with an emphasis on the more recent ones. This extends and updates the similar exercise of Ross [4]. Care has been taken to explicitly define the validity conditions for the applicability of the various theories, and to express the results in a form convenient for evaluation in relevant experimental conditions. The ability of the theoretical models to reproduce the observed transport properties of JET plasmas has then been assessed by comparing predicted transport coefficients with those inferred from the local energy balance, based on profile measurements for a large number of JET discharges.

The structure of this paper is as follows. The procedures used to analyze measured JET data for the purpose of comparison with theory are described in Section 2. Some discussion is given of observed experimental trends and of the importance of the inevitable uncertainties in the determination of local transport parameters. The assessment of theoretically predicted ion energy transport is given in Section 3 for toroidal η_i modes, and in Section 4 for trapped ion modes. Several theories of ion transport involving ion temperature gradient turbulence are described and discussed in general terms; their applicability to JET plasmas, and the stability properties of the measured profiles are examined. Finally, theoretically predicted transport coefficients are compared with those inferred from the experimental measurements. A discussion of the results obtained and overall conclusions are given in Section 5.

Definitions of all symbols used in this paper are given in the Appendix.

2. *Techniques for comparison with JET measurements*

Theoretically predicted heat fluxes or transport coefficients can be compared with those inferred by analyzing the local energy balance in JET plasmas. The basic measurements and the various steps in the derivation of "experimental" transport coefficients - and of physical parameters relevant to the theory of ∇T_i instabilities - are summarized for two JET discharges (one L-mode and one H-mode) in Figures 1(a-f) and 2(a-f).

Similar analyses have been carried out for a large number of JET discharges in different conditions; in this Section we discuss aspects of such analyses that are relevant to the assessment of theoretical models for ion energy transport.

a. *Measured profile data*

A complete set of experimental data, for the purpose of local transport analysis, is represented by space- and time-resolved measurements of electron and ion temperature and density, and of radiative power losses. Physics modelling calculations are used to identify the magnetic flux surface geometry (onto which the measured profile data are mapped) and to determine source terms such as Ohmic, neutral beam injection and radiofrequency heating.

The experimental information in the present paper has been obtained using a set of diagnostics measurements including the electron temperature from electron cyclotron emission spectra, the electron density from microwave interferometry and LIDAR Thomson scattering, the ion temperature and impurity concentration from charge-exchange recombination spectroscopy, and the radiated power density from bolometry. Examples of measured data are shown in Figures 1b and 2b.

In the majority of JET discharges, however, only a central ion temperature and a line-averaged effective ionic charge are measured. In such cases, assumptions are made concerning the corresponding radial profiles, ensuring consistency with the independent measurements of thermonuclear neutron yield and total plasma energy content. A uniform effective ionic charge and an ion temperature profile similar in shape to that of the electrons generally satisfy these constraints.

In order to evaluate theoretical predictions, we shall generally use the measured electron density profile *in lieu* of the ion one; for example, η_i will be defined as L_{n_e}/L_{T_i}, a prescription justified by the recent work by Mattor [5] where impurities are taken into account. The large majority of JET plasmas are characterized by monotonic density profiles; we shall not consider here the case of inverted density gradients observed in one specific regime of operation (high-density elm-free H-modes).

The plasma geometry is determined using the *mhd* equilibrium reconstruction code IDENTC [6]. We shall refer to a flux surface coordinate $0 \lesssim \rho \lesssim 1$, defined as the square root of the normalized poloidal magnetic flux. For most JET plasmas, ρ is an approximately linear function of the midplane minor radius of the plasma column.

The auxiliary power deposition profiles are modelled using the PENCIL [7] and PION [8] codes, for NBI and ICRF respectively. A local heat flux q can then be determined. A convective contribution $q_{conv} \equiv 3/2\ \Gamma\ T$ is subtracted, where the local particle flux Γ has been inferred separately by solving the particle balance (for all the cases considered here, q_{conv} is a minor fraction of the total heat flux, as exemplified in Figures 1d and 2d). The remainder of the heat flux is assumed to be conductive, $q_{cond} \equiv -n\chi\nabla T = q - q_{conv}$, and the thermal conductivity $\chi(\rho)$ appearing here is what will be compared with the theoretical predictions.

b. *Radial resolution of transport analysis*

The coarseness of the experimental profile measurements implies that estimates of χ - and of other relevant parameters such as η_i - for JET plasmas represent averages over 20-30 cm in radial extent (as shown in Figures 1e and 2e). Smaller structures cannot be resolved, and the comparison with theory thus relies implicitly on the assumption that highly localized transport effects are not dominant.

The lack of accurate measurements of plasma parameters and their gradients near the plasma edge limits the radial region over which reliable experimental information on local transport can be obtained in JET to exclude 10-20 cm from the outer plasma boundary. In addition, when sawteeth are present the transport properties in the inner 30-40 cm of the plasma column are also obscured by the dominance of *mhd*-induced energy losses.

In general, therefore, a meaningful comparison between theoretical and observed transport is possible within an intermediate radial range $0.4 \lesssim \rho \lesssim 0.8$, corresponding approximately to the region between the $q = 1$ and the $q = 2$ surfaces. For a significant minority of sawtooth-free plasmas, however, we are able to extend the comparison to the vicinity of the magnetic axis.

c. *Measurement of local ion heat transport*

When discussing anomalous ion transport, it is of course desirable to isolate the part of heat loss that can be attributed to the ions. This is in practice possible only in regimes of comparatively low density and high electron temperature, when the energy exchange rate between electrons and ions (assumed to be purely collisional) can be determined with sufficient accuracy.

This energy transfer term is often the main source of uncertainty in the inferred χ_i and χ_e; other contributions to the quoted error bars come from estimates of the sensitivity of the modelling calculations (*eg* auxiliary heating deposition profiles) to errors in the measured profiles.

In the examples of Figures 1 and 2 a separation of experimental electron and ion heat fluxes is possible. For higher density plasmas, it is generally not possible: in such cases, as well as in situations in which the ion temperature profile is not measured, a one-fluid thermal conductivity will

be quoted, defined as $\chi_{eff} \equiv -(q_e + q_i)_{cond} / (n_e \nabla T_e + n_i \nabla T_i)$, where n_i and T_i are modelled as described in Section 2a.

d. *Scaling of local energy transport in JET plasmas*

A comprehensive empirical description of the dependence of local energy transport on plasma and machine parameters in JET has not yet been obtained. Global energy confinement is known to scale favourably with the plasma current and unfavourably with the auxiliary input power, but the interpretation of this behaviour in terms of dependence of χ on local parameters is still being debated.

The current scaling may be due to a variation in the local shear length or simply in the poloidal magnetic field. An increase of χ with the plasma temperature may produce the power degradation; the density dependence of χ has however not yet been resolved, and it is possible that the relevant dependence is on pressure.

One definite feature of the local thermal conductivity in JET - as in other tokamaks - is its increase with radius towards the plasma edge, required to explain the observed bell-shaped temperature profiles. When ion and electron transport can be separated, this radial dependence is displayed in particular by ion thermal conductivity (as in Figures 1e and 2e), which differs from the neoclassical prediction [9] both in magnitude and in radial dependence.

e. *Data base used for the comparison with theoretical models*

In order to obtain statistically significant results, we shall use for our comparisons an extensive set of experimental data corresponding to well-diagnosed JET discharges with auxiliary heating.

In the scatter plots that will illustrate the comparison between modelled and observed transport, each data point will correspond to one discharge in approximate steady-state conditions, analyzed as described above. Most of the plasmas considered have been obtained in limiter L-mode discharges, but several H-mode discharges (obtained in the presence of a magnetic separatrix) are also included. A small number of data points correspond to high-performance regimes of special interest, such as the pellet-enhanced mode [10] and the hot-ion H-mode [11]. The relevance of the overall results of our assessment to these regimes will be discussed briefly in Section 5.

Transport in the hot plasma core ($\rho \lesssim 0.4$) will be examined using data from sawtooth-free discharges. For most of these, the ion temperature profile was not measured; consequently, when referring to this set of data we shall use χ_{eff} rather than χ_i as a measure of the observed heat transport.

For the outer plasma region ($\rho \gtrsim 0.5$), which is most important in determining global energy confinement, we shall instead use data selected by requiring not only that $T_i(\rho)$ be measured, but also that the

experimental determination of the local χ_i be sufficiently accurate (with an error bar not larger than $\pm$ 50%).

For each of the theoretical models considered, then, subsets of these data bases will be used for which the specific applicability conditions are satisfied. In some cases, the constraints to be imposed will be very restrictive, and the comparison with experiment will be possible only in specified regions of the radial domain.

3. *Toroidal η_i modes*

Instabilities driven by an ion temperature gradient are often characterized by the value of η_i, the ratio of density to temperature scale length, and are therefore often referred to as "η_i-modes". However, in the limit of uniform density ($\eta_i \to \infty$) the mode is characterized by a critical temperature gradient, and hence is also called a ∇T_i-driven mode. A whole family of these modes exists depending on the tokamak plasma conditions.

The most basic of the ∇T_i instabilites is the slab mode, which occurs as a result of ion acoustic waves coupling to a radial gradient in the ion pressure. Horton et al. [12] and Guzdar et al. [13] have considered the mode in toroidal geometry, where it was found that unfavourable curvature takes over from the acoustic waves as the main driving mechanism. The mode then has a different structure and becomes more "ballooning" in nature.

This leads to a natural categorization of the modes into either "slab" or "toroidal". As shown in the early work on the toroidal mode [12], the theories are valid in two different regions of parameter space: slab theory applies in the presence of short shear lengths $L_s \equiv Rq/\hat{s} < R/2$, while toroidal theory applies when $L_s > R/2$.

The inverse rotational transform q in tokamaks is close to unity near the magnetic axis, and increases with the plasma radius. Correspondingly, the dimensionless magnetic shear $\hat{s} = (r/q)\, dq/dr$ is close to zero (and largely uncertain) at the plasma centre, and becomes larger than unity in the outer region of the plasma column. Figure 3 shows radial profiles of the shear length for JET limiter discharges over a wide range in plasma current.

It is apparent that slab theory is generally not applicable to JET experimental conditions. The slab constraint may be satisfied, in the presence of a magnetic separatrix, near the very edge of the plasma. For this region, however, reliable quantitative information on the local transport behaviour is not available.

We will therefore not address slab theories specifically, and our study will focus on theories of the toroidal η_i mode.

When dealing with each model, we shall comment in some detail on their theoretical and physical basis, in order to provide understanding and allow an assessment of their value (some complementary aspects have been addressed recently by Horton [14]).

a. *Biglari et al.* [15]

These authors adopt a gyrokinetic treatment to study the stability of the toroidal mode, considering the cases of peaked and flat density profiles separately, in the collisionless regime.

The mode frequency is ordered like the magnetic drift frequency ω_{di}, so that collisions can be neglected if $\nu_{ii} < \omega_{di}$, leading to the constraint

$$\nu_{*i} < \varepsilon^{-3/2}\, q\, k_\theta \rho_i \ . \qquad (1)$$

With temperatures of several keV and density of a few $10^{19}\,m^{-3}$, JET plasmas are well into the collisionless regime, as can be seen in Figure 4. Thus, the condition Eq.(1) is generally satisfied across the radial domain of interest, as shown in Figure 5a, provided $k_\theta \rho_i > 0.1$.

The most limiting constraint, arising from the ordering adopted in [15], is

$$\omega_{di} > \omega_{bi}, \omega_{ti} \quad \rightarrow \quad k_\theta \rho_i > \frac{1}{q} \tag{2}$$

which for realistic mode spectra can never be satisfied in the core of the plasma column where $q \simeq 1$. However, the result of Eq.(2) is that the ion transit resonance can be neglected; and since Romanelli [16] has shown that this resonance has a small effect, one may be justified in dropping this constraint. Accordingly, we shall discuss also the prediction of transport near the plasma centre.

In the peaked density limit ($\omega_{*i} > \omega_{di} \rightarrow \varepsilon_n < 1/2$) Biglari et al. find instability for

$$\eta_i < 0 \text{ or } \eta_i > 2/3 \quad \text{and} \quad \varepsilon_T < \varepsilon_{Tc} \tag{3}$$

where ε_{Tc} is a critical value obtained by a numerical solution of the dispersion relation. Numerical solution for $k_\perp \rho_i = k_{/\!/} = 0$ gives the stability diagram in terms of ε_T and ε_n sketched in Figure 6. In the flat density limit, $|\varepsilon_n| \gg 1$, the mode is stable if

$$\varepsilon_T > \varepsilon_{Tc} \simeq 0.35 \tag{4}$$

The stability boundary for large ε_n can only be taken as qualitative, since it has been derived assuming, in effect, $q \rightarrow \infty$. As will be discussed below, however, Romanelli [16] finds that the threshold is independent of q, and obtains a similar value for ε_{Tc} assuming $k_\theta \rho_i \simeq 0.3$.

Dominguez and Waltz [17] analyzed the linear stability thresholds in the fluid limit for flat density profiles. Although the validity of the fluid limit may be questioned for threshold calculations, it is interesting to note that they found results in good qualitative agreement with [15], and showing that for increasing $k_\perp \rho_i$ the stability boundary is pushed to lower values of ε_{Tc}, as indicated by the arrow in Figure 6 .

Figure 7 shows the distribution of JET experimental data on this stability diagram. The plots include data from sawtooth-free L-mode plasmas in deuterium, and refer to various radial positions in the plasma. It can be seen that - if the stability boundaries from [15] are taken at face value - the majority of data points for the plasma core region (where the flat density limit more often applies) lie well inside the unstable region. The region close to the $q = 1$ surface is where the maximum temperature gradients are usually attained in the absence of sawteeth.

Nearer the plasma edge the density scale length is generally much reduced; nevertheless, most of the plasmas are still unstable according to the criterion in Eq.(3).

One should therefore expect the anomalous ion transport from the toroidal η_i mode to contribute to the observed heat fluxes. Biglari et al. derive an expression for the ion thermal conductivity using the fluid equations and employing mixing length estimates:

$$\chi_i = \frac{c_s \rho_s^{\,2}}{R} (k_\theta \rho_s) \frac{L_s}{L_n} \frac{(1+\eta_i)}{\tau} \qquad (5)$$

Because of the fluid approximation, we are limited to considering situations where $\eta_i \gg 1$.

An upper bound on $k_\theta \rho_i$ of $(1+\eta_i)^{-1/2}$ (as obtained from a linear analysis) has been used in the following comparisons to obtain a simple expression for the upper limit of χ_i. Work performed by Sydora et al. [18] where a non-linear calculation of the spectrum was performed suggests that the important range of $k_\theta \rho_i$ is $0.1 < k_\theta \rho_i < 0.5$, thus indicating that this upper bound on χ_i could be close to the actual value.

In Figure 8a we show a comparison of predicted and measured thermal conductivity for the same data set as in Figure 7. The data refer to the plasma core ($\rho \simeq 0.3$), which corresponds to having relaxed the theoretical constraint Eq.(2). Also, the quantity inferred from the experimental data is here an "effective" thermal conductivity, since spatially resolved ion temperature measurements were not available in most instances. It is nevertheless apparent that the theoretical χ_i largely overestimates the observed transport in almost all cases.

If all applicability criteria for the theory are strictly enforced, the comparison is possible only for larger plasma minor radii. This is shown in Figure 8b for a set of discharges for which the experimental estimate of χ_i is believed to be reliable (the error on it being less than $\pm$ 50%). Data are plotted for three different radial positions in the "confinement region" ($\rho = 0.50$, 0.65 , 0.80); locally $\varepsilon_n < 1/2$ for all plasmas.

The anomalous ion transport due to the toroidal η_i mode decreases towards the plasma edge, and is clearly anti-correlated in radial behaviour to the measured one. A degree of correlation appears to exist at each radial position, indicating that model and observations may have some common parametric dependence. A qualitatively similar result is obtained when the comparison is carried out for data to which the flat density limit applies.

b. *Guo et al.* [19]

In this paper the fluid limit of the electrostatic gyrokinetic equations is used for flat density profiles. The linear growth rate - needed for the mixing length estimate of χ_i which this paper reports - is calculated assuming $\varepsilon_T \ll 1$ which, as we have seen, is generally justified for JET parameters. Stability boundaries are not discussed, but the assumptions mentioned implicitly point to η_i being much larger than a critical value of order unity.

Two expressions for χ_i are then calculated in two different wavelength regimes, the weak ballooning limit ($b_\theta \equiv (k_\theta \rho_s)^2/\tau \ll \varepsilon_T^{1/2}$) and the strong ballooning limit ($\varepsilon_T^{1/2} \ll b_\theta \ll 1$). For b_θ small, χ_i is found to be an increasing function of b_θ, whereas in the second range χ_i is a decreasing function of b_θ. From these results, Guo et al. predict that a maximum of χ_i must exist between the two b_θ limits, and that the value of b_θ for which this maximum occurs is the most important value for transport. Approximating this value to be where the predictions for χ_i in the two limits are equal gives

$$b_\theta \simeq \left[\frac{2\varepsilon_T}{q\tau\hat{s}(1+2q^2)} \right]^{1/2}$$

leading in practice to mode wavelengths of the order of the ion Larmor radius. Here, strictly speaking, q represents the cylindrical safety factor.

The corresponding value of χ_i is

$$\chi_i = 0.6 \frac{c_s {\rho_s}^2}{R} \frac{(1+2q^2)^{3/4}}{(\hat{s} q {\varepsilon_T}^3 \tau^3)^{1/4}} \tag{6}$$

This is compared with measured data in Figures 9a and 9b. In the "confinement region", a limited number of data points have been selected by requiring $\varepsilon_n > 1$ (flat density limit). While χ_i is on average lower than that predicted by Biglari et al., the discrepancy in the plasma core remains significant. The radial dependence of χ_i remains dominated by the leading term ($\sim T_i^{3/2}$); the additional q-dependence is not sufficiently strong to induce the necessary increase near the edge.

c. *Hong and Horton* [20]

Hong and Horton solve the 2D fluid equations describing the toroidal η_i instability and use mixing length estimates to derive the ion thermal conductivity. The fact that fluid equations have been used implies that the results can only be applied to conditions in which η_i is far above a threshold $\eta_{i,c} \simeq 2/3$.

Two expressions for χ_i are derived, with different scalings. One corresponds to very low shear, $\hat{s} < \rho_s/L_n$, a condition that can only be satisfied in the immediate vicinity of the magnetic axis, where the experimental information is insufficient to test the model.

In the higher shear limit, $\rho_s/L_n < \hat{s} < 2\varepsilon_n$, on the other hand, the predicted

$$\chi_i = 2 \frac{c_s {\rho_s}^2}{R} \frac{[\eta_i - 2/3]^{1/2}}{\hat{s}\tau^{1/2}} \tag{7}$$

can be compared with data over a wide radial range. This is done in Figures 10a and 10b , with results that again indicate an overestimate of

transport in the plasma core and a tendency to a decrease with radius, with no apparent correlation between predictions and observations in the confinement region.

d. *Dominguez and Waltz* [21]

Using a modified mixing length approximation [12], Dominguez and Waltz identify - for $k_\perp \rho_s \sim 0.3$ - a stability boundary broadly described by

$$\varepsilon_{Tc} \simeq [\, \varepsilon_n \,, 0.25 \,]_{\min}$$

ie similar to that of Biglari et al. [15]. The temperature profile peaking required for instability is somewhat higher than in Figure 6, but most JET L-mode plasmas are still unstable, as illustrated in Figure 7.

For plasmas that are well into the unstable domain, the ion thermal conductivity is predicted to have the form

$$\chi_i \simeq 3.53 \, \frac{c_s \rho_s^{\,2}}{R} \, \frac{L_s}{L_{T_i}} \left[1 - \frac{\varepsilon_T}{\varepsilon_{Tc}} \right]^{1/2} \tag{8}$$

When compared with a subset of JET data selected to satisfy the model's applicability conditions, the predicted χ_i is found to be largely in excess of the experimentally determined one in the inner plasma, and displays a strong opposite radial dependence (Figure 11).

e. *Hong et al.* [22]

This paper extends the earlier work by Horton et al. [12] to include kinetic effects. Ions are described by gyrokinetic theory, with adiabatic electrons; the ordering used is $\omega \gg \omega_{di} > k_{//} v_{ti}$. Using an expression for $k_{//}$ derived in [12], and the fact that in their analysis Hong et al. find $\omega \sim k_\theta \rho_i c_s / L_n$, these two constraints lead to

$$\varepsilon_n \ll (\tau/2)^{1/2} \quad \text{and} \quad \frac{R}{L_s} \, \frac{(1+\eta_i)^{1/2}}{\varepsilon_n^{\,1/2}} \ll 1$$

With these restrictions and also $\eta_i \gtrsim 2$, Hong et al. derive the following expression for χ_i :

$$\chi_i = 2 \, \frac{c_s \rho_s^{\,2}}{R} \, \frac{L_s}{L_n} \, \frac{(1+\eta_i)}{\tau^{1/2}} \, f(\varepsilon_n, \eta_i, \tau) \tag{9}$$

where f is a complicated function of peaking parameters and temperature ratio [22] which cannot be summarized by a simple scaling.

The applicability of this model to JET plasmas is very limited, mainly because of the stringency of the constraint on the local shear, only satisfied in practice near the centre of discharges with sufficiently peaked density profile. A comparison with such a subset of the data used above

is shown in Figure 12, and indicates once more that the predicted transport is very much larger than the observed one.

f. *Romanelli* [16]

The toroidal η_i mode is treated here by solving the gyrokinetic drift equation numerically, retaining the ω_{di}/ω resonance. Using a fluid limit of the equations, Romanelli demonstrates the ordering $\omega \sim \varepsilon_n^{1/2}\omega_{*i}$. The fact that collisions have been neglected leads to the constraint

$$\nu_{*i} < \varepsilon^{-3/2}\, q\, k_\theta \rho_i \,/\, \varepsilon_n^{1/2} \tag{10}$$

This is even weaker than that discussed above for the theory of Biglari et al., and is therefore always easily satisfied (see Figure 5b).

A threshold for instability is obtained by fitting numerical solutions of the gyrokinetic equations as

$$\eta_{i,c} = 0.5 + 2.5\,[\varepsilon_n\,,\ 0.2]_{\max} \tag{11}$$

This corresponds to a stability boundary, in the diagram of Figure 6 not dissimilar from that obtained by Biglari et al., with $\varepsilon_{Tc} = 0.4$ in the flat density limit. Again, therefore, one should conclude that JET plasmas tend to lie well into the unstable region, as shown in Figure 7.

Romanelli uses a quasilinear mixing length estimate to derive an expression for χ_i due to η_i transport using a kinetic response and without expanding in ω_{di}/ω. Because kinetic effects are kept, the theory is valid down to very low η_i, close to the threshold value. Restrictions imposed on the calculation of the ion energy flux lead to the requirement $\varepsilon_T \ll 1$ which, as we have seen, is generally satisfied by JET profiles. Taking $k_\theta \rho_i \simeq 0.3$, Romanelli gives

$$\chi_i = 14\,\frac{c_s {\rho_s}^2}{R}\,\frac{(\eta_i - \eta_{i,c})^{1/2}}{\varepsilon_n^{1/2}\tau^{3/2}} \tag{12}$$

with $\eta_{i,c}$ given by Eq.(11).

This prediction can be compared with a large number of JET data to which the model is found to be applicable. The results are shown in Figures 13, and are very similar to those obtained before for the model by Biglari et al. - except that here theory and experiment appear to be rather uncorrelated also at individual radial positions.

In a later work with Briguglio [23], Romanelli uses kinetic theory to investigate the microinstabilities that are driven by trapped electrons and ion temperature gradients. The corresponding expressions for instability threshold and thermal conductivity are rather complicated, involving explicit scalings with local aspect ratio, ion/electron temperature ratio and collisionality, as well as with the profile peaking parameters. We shall not report them here, to avoid transcription errors, and refer the interested reader to Appendix C of [23].

Having evaluated them for JET plasma conditions, we find that the model is again very generally applicable. A comparison with measured transport qualitatively reproduces the results in Figure 13, except for a reduction in χ_i that brings it closer to the observed values in the intermediate radial region, while still remaining a large overestimate near the plasma centre.

g. *Romanelli, Chen and Briguglio* [24]

This more recent article describes a kinetic theory of the ion temperature gradient driven mode in the limit of long wavelength. The calculation in toroidal geometry leads to the identification of two modes that can contribute significantly to transport.

The first ("ion toroidal mode") propagates in the ion diamagnetic drift direction, and is shown to be unstable whenever $\eta_i > 2$ and

$$\lambda \equiv \frac{q\, k_\theta \rho_i}{\varepsilon_T \sqrt{2}} \quad > \quad \lambda_c \equiv \left[\frac{\eta_i}{2\tau^2} \frac{1+\tau}{\eta_i - 2} \right]^{1/2} \tag{13}$$

The wavelengths considered are such that $k_\theta \rho_i \sim \varepsilon_T$.

The following thermal conductivity is given without an explicit derivation:

$$\chi_i \simeq \frac{c_s \rho_s^{\,2}}{R} \; \frac{q}{4\tau^{3/2} \hat{s}^2 \varepsilon_T} \tag{14}$$

An attempt to re-derive it leads us to a different shear dependence, $\hat{s}^{-1}$ rather than $\hat{s}^{-2}$. The discrepancy is, however, academic since hardly any JET data can be found to which this model is applicable. The condition $\lambda > \lambda_c$ requires q significantly greater than unity, but towards the plasma edge (where this constraint can be satisfied) it is very unusual to have values of $\eta_i > 2$.

Another mode found by Romanelli, Chen and Briguglio has a slab-like analogue, and is therefore termed "slab mode". This is considered in the ordering $k_\theta \rho_i \lesssim \varepsilon_T^{1/2}$, *ie* shorter wavelengths are allowed than for the toroidal calculation. By assumption, λ should be constrained as

$$\lambda_0 \ll \lambda \ll \lambda_0^{-1/4}, \quad \text{where} \quad \lambda_0 = 7\,\pi^{1/2} (\varepsilon_T \hat{s} \tau)^2 \tag{15}$$

and the density profile should be sufficiently flat, so that

$$\eta_i \gg \frac{32}{7\pi^{1/2}} \frac{\tau^{3/5} \lambda^{1/5}}{\varepsilon_T^{\,2/5} \hat{s}^{2/5}} \tag{16}$$

The first of these conditions can be satisfied, in practice, only in the central portion of the plasma column where $q \simeq 1$ and the shear is small. For this region, and for plasmas satisfying the second constraint, we have evaluated the mixing length estimate of χ_i (given in [24] without derivation):

$$\chi_i \simeq \frac{c_s \rho_s^{\,2}}{R} \; \frac{q}{4\tau(\hat{s}\varepsilon_T)^{1/2}} \tag{17}$$

The comparison with the observed transport in the plasma core, given in Figure 14, shows a poor correlation, but the magnitude of χ_i from Eq.(17) at least is larger than the measured one only by a factor $\sim 2 \rightarrow 4$.

h. *Kim et al.* [25]

We complete our discussion of the toroidal η_i mode with this work in which the transport due to a temperature gradient mode in a neo-classical fluid model is considered. The imposed frequency ordering $\omega \sim \omega_{*i} \ll \omega_{bi}$ leads to the restriction

$$\tau^{1/2}\varepsilon^{1/2}\varepsilon_n/q \gg k_\theta \rho_s / \sqrt{2} \sim 0.2 \tag{18}$$

which is satisfied when the density profile is sufficiently flat. The low collisionality constraint, as usual, is easily satisfied.

An upper bound on χ_i is then obtained from the neoclassical fluid equations in the form of a neoclassical coefficent enhanced by a factor $(1 + \eta_i)$:

$$\chi_i \lesssim 2.3 \frac{0.78\varepsilon^{1/2}\nu_{ii}}{1 + 0.44\nu_{*i}} \frac{\rho_s^{\,2} q^2}{\varepsilon^2} (1 + \eta_i) \tag{19}$$

In JET, unfortunately, the ion energy transport is so largely anomalous that even this enhanced neoclassical coefficient generally remains far too small to account for the observed heat flux, as shown in Figure 15.

4. *Trapped ion modes*

In the theoretical study of ∇T_i-driven instabilites, consideration of toroidicity introduces a further complication - the trapped particles which exist as a consequence of inhomogeneity in the magnetic field (with the stronger field on the inboard side of the torus). Because these particles are confined to the outboard side they respond differently to perturbations compared with the passing particles which transit the whole magnetic surface. This gives rise to a new class of instabilities, called the "trapped ion modes" [26], which can be driven unstable by the temperature gradient.

These modes can be categorized according to the value of η_i [15]. For low η_i (close to zero) the mode is described as "dissipative" and is driven unstable by electron collisions, which are able to tap the energy source of the passing particles. This region is interesting, because although electron collisions destabilize the mode, it is found that ion collisions have a stabilising influence [26]. As η_i is increased above the value of 4/3, the mode characteristics alter. The most significant change is that ion collisions now become destabilising, tapping the energy source of the ion pressure gradients. Finally, at large η_i ($\gtrsim O(\varepsilon^{-1/2})$) the mode becomes independent of particle collisions and is fluid-like in nature.

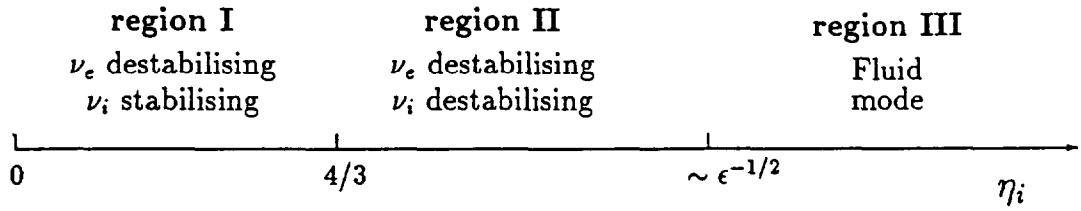

Figure 16 : Mode properties as a function of η_i

These results are summarized in Figure 16. Due to the influence of the ion collisions, it is found that the transport in region II is significantly larger (by factors of the order $(m_i/m_e)^{1/2}$) than that in region I.

We now proceed to discuss various trapped ion transport models that have been put forward recently.

a. *Diamond and Biglari* [27]

Earlier work on dissipative trapped ion convective cell turbulence (driven by electron collisions) [28] is reconsidered here. In the earlier work, Cohen et al. had dropped the two-dimensional ***ExB*** advective non-linearity (but retained non-linearity via a one-dimensional "shock" term); they then derived a diffusion coefficient that scaled as $D \sim T^{21/2}$, thus leading to a very large anomalous transport, particularly at high temperatures. However, when the temperature is high the ***ExB*** term is the dominant non-linearity, and this work of [28] becomes invalid.

Biglari and Diamond consider this regime of low electron collisionality - which is appropriate for JET plasma conditions - where the ***ExB*** term

dominates, and they drop the shock non-linearity. This then leads to a two-dimensional equation describing the mode. They claim that such an equation is better able to transfer the unstable fluctuation energy to the sink (where it can be dissipated) than the one-dimensional version. In other words, a two-dimensional system is able to support a steady state with less transport than a one-dimensional system, and the characteristic thermal conductivity is:

$$\chi_i = \frac{3}{2\sqrt{2}} \frac{c_s \rho_s^{\,2}}{L_n} (m_e/m_i)^{1/2} \frac{\varepsilon^{1/2}}{\hat{s}^2} \frac{q}{\varepsilon_n \nu_{*e}} \qquad (20)$$

This transport coefficient features additional dependences to those typical of the toroidal η_i modes; in particular, the scalings with aspect ratio and density scale length might be expected to go some way towards improving the radial behaviour of the predicted transport. In fact these are compensated by the dependences on shear and collisionality, and the result is still in conflict with the observations, as can be seen from Figure 17. In the plasma core, the predicted transport varies by orders of magnitude (with the highest values corresponding to lowest collisionality) with JET experimental conditions, whereas only a modest variation is observed. Towards the plasma edge, the trapped ion mode transport becomes rapidly negligible, and shows no correlation with the measurements.

The same authors consider the trapped ion temperature gradient driven mode using a two-point renormalized (clump) theory in [29]. The mode - which is shown to propagate in the ion drift direction - is driven by unfavourable magnetic curvature, unlike the "conventional" slab η_i mode which is driven by a sound wave and propagates in the electron drift direction. Whilst the ions are treated using clump theory, the electrons are assumed to be sufficiently collisional that electron clumps are not formed. This imposes the constraint on electron collisionality:

$$\nu_{*e} \gg \frac{k_\theta \rho_s \, q \eta_i}{2\varepsilon^{1/4} \hat{s} \varepsilon_n \tau} (m_e/m_i)^{1/2} [\eta_i - 2]^{1/2} \quad , \text{with } \nu_{*e}, \nu_{*i} \ll 1$$

while the other frequency orderings require

$$\varepsilon_n \ll 1 \quad (\omega_{*i} \gg \omega_{di}) \qquad \text{and} \qquad k_\theta \rho_s \ll (2\varepsilon\tau)^{1/2} \varepsilon_n / q \quad (\omega_{bi}, \omega_{ti} \gg \omega_{*i}) \qquad (21)$$

These constraints can be satisfied, for JET parameters, only by assuming that the modes have very long wavelengths, $k_\theta \rho_s < 0.1$. The requirement of a large η_i with peaked density profile strongly restricts the range of JET data to which the model is applicable, as can be seen from Figure 7.

A model thermal conductivity can be derived from [29] assuming $\omega \sim \omega_{di}$:

$$\chi_i \simeq \frac{1}{2\sqrt{2}} \frac{c_s \rho_s^{\,2}}{L_n} (m_e/m_i)^{1/2} \frac{q \eta_i^{\,2}}{\varepsilon_n \nu_{*e} \hat{s}^2 \tau^2} [\eta_i - 2] \qquad (22)$$

This is very similar to Eq.(20), with an additional strong dependence on η_i which - for unstable plasmas - is bound to yield even stronger disagreement with observations than that of Figure 17.

b. *Biglari et al.* [15]

This work, which we considered earlier in Section 3 in relation to the toroidal η_i mode, also calculates transport due to the trapped ions. Trapped ion ∇p_i-driven modes are considered first in a collisionless model, and then for a model where the part of the collision operator which describes pitch angle scattering is included. The frequency ordering is analogous to that just discussed, leading to the same constraints Eq.(21) and to the corresponding limitations on applicability to JET plasma regimes.

For the collisionless case, a criterion for instability is derived which is

$$\eta_i > \eta_{i,c} = \frac{\varepsilon^{1/2}\tau^2}{2\sqrt{2}\,\varepsilon_n(1+\tau)} - 1 \tag{23}$$

In JET, plasmas are found to be unstable when the density profile, while not being flat, is also not too peaked ($\varepsilon_n \sim 1/3$).

The following (mixing length) form is then predicted for the ion thermal diffusivity (falling into the fluid region of the mode, *ie* region III of Figure 16):

$$\chi_i \simeq 2^{3/4}\,\frac{c_s\rho_s^{\,2}}{L_n}\,\frac{\varepsilon^{1/4}\varepsilon_n^{\,1/2}}{k_\theta\rho_s\,\hat{s}^2}\,[1+\eta_i/\tau]^{1/2} \tag{24}$$

When compared with JET data, under the assumption of long wavelength modes ($k_\theta\rho_s < 0.1$ has to be enforced, in order for the model to be applicable), this prediction is found to be a large overestimate of the observed transport in the plasma core, as shown in Figure 18. The usual decline in the theoretical χ_i with radius leads to a "cross-over" with experimental data at $\rho \sim 0.8$.

Biglari et al. then study the effect of perturbatively including ion collisions via a pitch angle scattering operator. An early work [26] had found that the dissipative trapped ion mode was stabilised by ion collisions; there, $\eta_i = 0$ was assumed, falling into region I of Figure 16. Here the finite η_i regime is explored, and it is found that beyond a critical value of η_i ion collisions actually have a destabilizing influence (region II). Thus when

$$\eta_i > \frac{4}{3} \quad \text{and} \quad \nu_{*i} < q\,k_\theta\rho_s\,\frac{\tau^{1/2}}{\varepsilon_n^{\,1/2}\varepsilon^{1/4}} \tag{25}$$

the mode is unstable and the thermal diffusivity is of the form

$$\chi_i = 2\sqrt{2}\ \frac{c_s \rho_s^{\ 2}}{L_n}\ \frac{\eta_i q \tau^{1/2}}{\hat{s}^2 \varepsilon^{1/4} \nu_{*i}} \qquad (26)$$

JET plasmas are found to be often unstable according to the criteria in Eq.(25), even for rather long mode wavelengths ($k_\theta \rho_s$ down to ~ 0.1). The model Eq.(26) is thus widely applicable to JET data, but it predicts transport several orders of magnitude larger than that observed - the inverse dependence on the ion collisionality adding to the usual shortcomings of previously considered models.

c. *Xu and Rosenbluth* [30]

These authors have considered the stability criterion for the trapped ion modes and its relation to certain other instabilities. Considering low-frequency, long wavelength modes a general analytic dispersion relation is derived which contains three types of instability: electrostatic trapped ion modes, magnetic trapped ion modes and *mhd* ballooning instabilities. The dispersion relation is obtained using a variational approach constructed from gyrokinetic equations; it is found that the couplings between the modes are weak, except for the case of the ballooning mode, where they find that the trapped particles act so as to give a stabilising contribution to the mode. By considering different mode frequency orderings they are able to separate out the trapped ion modes and evaluate thermal diffusivities and stability criteria for different collisionality regimes. The effects of collisions are incorporated into the model via a pitch angle scattering operator, but the effects of trapped electrons are not considered. We shall concentrate here on the results they obtain for the trapped ion modes.

The electrostatic mode is considered in region II of Figure 16. Xu and Rosenbluth derive thermal diffusivities for two collisionality regimes. For the collisionless case, the drift frequency must greatly exceed the ion collisionality, thus giving

$$\nu_{*i} \ll a_1 \frac{\sqrt{2}\ q\, k_\theta \rho_s}{\varepsilon^{1/2} \tau^{1/2}} \qquad (27)$$

$$\text{where } a_1 = 0.36 + 0.21\hat{s} - 0.21\left(1 + \frac{7}{6q^2}\right)\alpha \ , \quad \alpha = -q^2 R \frac{d\beta}{dr}$$

and β is the ratio of thermal to magnetic energy. The frequency ordering which they impose gives the following constraints on the mode wavelength:

$$\frac{\tau^{1/2} \varepsilon^{1/2} \nu_{*i}}{\sqrt{2}\, q} \ll k_\theta \rho_s \ll \frac{\tau^{1/2} \varepsilon^{3/4}}{\sqrt{2}\, q} \qquad (28)$$

For the JET plasmas which we have considered, both the above conditions are satisfied over a wide radial region, provided the modes are taken as having sufficiently long wavelength ($k_\theta \rho_s \lesssim 0.1$).

Xu and Rosenbluth find that the mode - which is driven by the ion pressure gradient - is unstable for α below a critical value

$$\alpha_c = (1.71 + \hat{s}) \left[1 + \frac{7}{6q^2} \right]^{-1} \tag{29}$$

a condition that is always easily satisfied for JET plasma profiles. The ion thermal diffusivity in this region can be estimated as

$$\chi_i = 2\sqrt{2}\ \frac{c_s {\rho_s}^2}{L_n}\ \frac{\varepsilon^{3/4} {a_1}^{3/2} \eta_i^{1/2} q {\varepsilon_n}^{1/2}}{\tau^{3/2} \nu_{*i} < H(\theta) >} \tag{30}$$

where for the purpose of our one-dimensional analysis we have taken a flux surface average of the poloidally varying prescription of [30]:

$$< H(\theta) > \equiv < 1 + h^2(\theta) > \quad , \text{ where } \ h(\theta) = \hat{s}\theta - \alpha \sin\theta \tag{31}$$

The transport coefficient given by Eq.(30) generally has a modest radial variation, since the combined dependences on aspect ratio, q and shear compensate for the decrease in the leading term with radius. Its magnitude, however, is between one and two orders of magnitude larger than that observed in JET, as shown in Figure 19. The large vertical scatter in this plot furthermore indicates that the observed transport is much less sensitive to variations in the parameters appearing in Eq.(30) than would be implied by the theoretical functional dependence of χ_i.

For the collisional case (where the collisionality greatly exceeds the drift frequency) the opposite limit to Eq.(27) must be satisfied, together with a separate bound on the mode wavelength imposed by the frequency ordering:

$$k_\theta \rho_s \gg \frac{\varepsilon_T \nu_{*i} \tau^{1/2}}{\sqrt{2}\, q} \tag{32}$$

Together, these two conditions imply in practice that this theory is applicable to JET only if the modes are assumed to have wavelength comparable to the plasma minor radius ($k_\theta \rho_s \sim 0.01$). The thermal conductivity is then given as

$$\chi_i = 2\sqrt{2}\ \frac{c_s {\rho_s}^2}{L_n}\ \frac{\varepsilon^{3/2} q \eta_i^2}{\nu_{*i} \varepsilon_n < H(\theta) > \tau^{3/2}} \tag{33}$$

(We observe incidentally that - even accepting as plausible the mode wavelength range required to make this model applicable - it is quite puzzling that the two electrostatic results just discussed should not agree

with the collisional result of [15], Eq.(26). Although there are similarities, several dependences are significantly different).

When evaluated for JET parameters, the collisional model Eq.(33) yields even larger transport (and discrepancy with observations) than the collisionless version tested above.

Finally, we turn to the purely magnetic mode (*ie* a mode in which there is no electrostatic contribution). The frequency ordering here is such that the following constraint should be satisfied:

$$k_\theta \rho_s \gg \sqrt{2}\, \frac{\varepsilon_n \varepsilon^{1/2} \nu_{*i} \tau^{1/2}}{q} \tag{34}$$

The stability condition can be expressed as a constraint on the collisionality; the mode then is unstable if

$$\nu_{*i} < 5.7 a_1^{1/2} [\beta(1 + 3\eta_i)]^{1/2} \frac{k_\theta \rho_s q}{\varepsilon^{1/4} \tau^{1/2} \varepsilon_n^{1/2}} \tag{35}$$

Both the above conditions are fulfilled in practice by a large number of JET data points, provided the mode wavelength is not too long ($k_\theta \rho_s \gtrsim 0.1$). The ion thermal conductivity to be assessed is then

$$\chi_i = 2\sqrt{2}\, \frac{c_s \rho_s^2}{L_n}\, \frac{a_1 q \beta (1 + 3\eta_i)}{\nu_{*i} < H(\theta) > \tau^{3/2}} \tag{36}$$

This is compared with experimental data in Figure 20: as usual, the predicted transport is too large in the plasma core. In the confinement region of JET plasmas, χ_i from Eq.(36) has on average the correct magnitude, but no correlation with the observed trends is apparent.

d. *Garbet et al.* [31]

To complete our review, we consider this work in which a dispersion relation is derived which describes three modes. Two of these are associated with the circulating particles and correspond to the η_i mode and to an interchange-type mode. The third is a trapped ion mode; the dispersion relation is solved numerically in the collisionless limit and within the framework of the ballooning formalism. Based on realistic two-dimensional *mhd* equilibria, the stability of plasmas with parameters and profiles representative of JET experimental conditions is investigated, for different values of the toroidal mode number n.

The results for the trapped ion mode are summarized by the stability diagram in Figure 21. The stability boundary is defined at low ε_n by $\eta_{i,c} \simeq 2/3 \rightarrow 1$ (depending on the value of n) and at large ε_n by a critical temperature gradient corresponding to $\varepsilon_{Tc} \simeq 0.10 \rightarrow 0.17$ (with the extreme values corresponding to $n = 30$ and $n = 150$, respectively). This

threshold is significantly lower than that quoted above for the toroidal η_i mode, and sketched in Figure 6.

In fact, it is important to note that Garbet et al. find for the η_i mode due to the circulating particles a critical value of $\varepsilon_{Tc} \sim 0.01$, in stark contrast with the results discussed previously. In practice, JET plasmas would then always be stable against the toroidal η_i mode, and trapped ion modes would be the sole plausible candidates for the explanation of anomalous ion transport. No estimate is given for the associated thermal conductivity, but one can see from the experimental data in Figure 7 that taking into account the uncertainties in the measurements, and depending on which toroidal mode number is regarded as dominant, JET plasmas might well be kept always at marginal stability by these modes. Advances in the theory are clearly required in order to reach a more quantitative assessment.

5. *Discussion of results and conclusions*

Anomalous ion heat transport has been shown in recent years to be an important aspect of energy confinement in tokamaks, for which a theory-based description would clearly be desirable, in particular when predictions are needed for the extrapolation of present-day plasma regimes to reactor-relevant conditions.

∇T_i-driven instabilities have been proposed as a candidate explanation and much theoretical effort has been devoted to their study, leading to a variety of predictions for the associated local transport as a function of the plasma parameters. Several such models have been tested here in the light of experimental measurements of local transport in JET.
(Recently Guo and Romanelli [32] have carried out a new and comprehensive stability analysis of the ∇T_i modes in various parameter domains. The resulting dependences of $\eta_{i,c}$ and the characteristics of the modes on q, τ and ν_* may be significant and merit comparison with JET data in the future).

We have seen that the assumptions made in deriving the theoretical models often significantly limit the extent to which they are applicable, in realistic JET operating conditions. Nevertheless, the domain of applicability of most models is sufficiently wide to allow comparison with measured data over a range of discharges, and at different radial locations across the plasma column.

As a result of these comparisons we find that, while specific models may vary as to the magnitude and functional dependence of the predicted transport, toroidal η_i and trapped ion mode theories share a fundamental qualitative shortcoming - the inability to describe the radial variation of the observed transport. The lack of correlation in this respect between theoretical predictions and experimental data is summarized in Table I.

According to most of the proposed theoretical stability criteria, the hot plasma core of JET sawtooth-free plasmas is unstable with respect to ∇T_i-driven modes. The ion thermal conductivity in this radial region should, then, be much larger than that inferred from the measurements (the difference going well beyond the uncertainties inherent in the analysis).

The predicted χ_i values are in fact such that - with the modest density profile peaking usually obtained in JET L-mode and H-mode discharges - one would never expect to see a departure from marginally stable temperature profiles, characterized by a much lower ∇T_i than that observed experimentally. In particular, if these modes were present it would have been impossible to achieve the high central ion temperature and thermonuclear performance of JET's preliminary tritium experiment [11], or the extreme temperature gradients observed in the core of JET plasmas following central fuelling by injection of frozen deuterium pellets [10].

Conversely, in the plasma region closer to the edge the theoretically predicted anomalous transport tends to vanish, either because the instability thresholds

are not exceeded, or because, when they are, χ_i is strongly reduced - in contrast to observations.

Indeed, for nearly all the models examined, the "leading term" in the thermal conductivity, $c_s\rho_s^2/R \sim T^{3/2}$, represents the main source of radial dependence for the theoretical χ_i. The additional parameteric dependences encountered can never overcome this decrease in transport with the plasma minor radius. Some in fact - notably, the inverse dependence on magnetic shear and plasma collisionality featured by several models - tend to make the discrepancy with the observed trend worse.

Beklemishev and Horton [33] have claimed recently that the radial variation of the density of states (*ie* Fourier modes) might explain the experimentally observed increase of transport near the plasma edge. However their discussion involves a number of assumptions which have not been justified by non-linear calculations.

For the models that have been considered here, it is of course possible to assume that, in the outer plasma region, some physical mechanism other than ∇T_i-driven instabilities is producing the anomalous ion energy transport required to explain the observations. Since that region is most important in determining the plasma's overall confinement, one should then not expect to see a correspondence between the global energy confinement scaling in JET and the parametric dependences of the local theoretical χ_i's that have been considered in this paper.

Acknowledgments

This work was undertaken under a JET Task Agreement as part of a joint collaboration between JET and AEA Fusion on comparing theories of anomalous transport with JET data and is partially funded by the United Kingdom Department of Trade and Industry.

The authors wish to acknowledge the encouragement and support of D.F.Duchs and M.Keilhacker, and useful discussions with J.G.Cordey, M.Ottaviani and A.Taroni on the subject of this paper.

Table I

A statistical measure of the correlation in radial behaviour between theoretical and experimental χ_i has been constructed using data taken at different radial positions in the plasma "confinement region", as for example in Figure 8b. For each such plot, the *Pearson coefficient* determines the conformity of the data to a linear relationship (as would be appropriate for a correct model), regardless of the relative magnitude of χ_i^{TH} and χ_i^{exp}.

The coefficient varies from +1 for a perfect positive correlation, to -1 for complete anti-correlation. A value of zero indicates no detectable correlation. All values quoted have a high level of significance (to $\lesssim 5\%$).

χ_i^{TH} *model*	*ref. in the text*	*Figure number*	*sample size*	*Pearson coefficient*
Biglari et al. [15]	Eq.(5)	Fig.8b	76	−0.32
Guo et al. [19]	Eq.(6)	Fig.9b	25	−0.16
Hong and Horton [20]	Eq.(7)	Fig.10b	148	−0.07
Dominguez and Waltz [21]	Eq.(8)	Fig.11b	108	−0.61
Romanelli [16]	Eq.(12)	Fig.13b	150	−0.41
Kim et al. [25]	Eq.(19)	--	82	0.02
Diamond and Biglari [27]	Eq.(20)	Fig.17b	51	−0.09
Biglari et al. [15]	Eq.(24)	Fig.18	121	−0.15
Xu and Rosenbluth [30]	Eq.(30)	Fig.19	75	0.08
Xu and Rosenbluth [30]	Eq.(33)	--	75	0.11
Xu and Rosenbluth [30]	Eq.(36)	Fig.20b	162	−0.05

Appendix

We list here the definitions of all non-standard variables used in this paper and not explicitly defined in the text. All parameters are averaged over magnetic flux surfaces (for example the local inverse aspect ratio is $\varepsilon = < r > / < R >$).

flux surface coordinate	$\rho = \sqrt{\psi_n}$ $\psi_n =$ normalized poloidal flux
temperature ratio	$\tau = T_e/T_i$
thermal velocity (species j)	$\mathbf{v}_{tj} = \sqrt{T_j/m_j}$
sound speed	$c_s = \tau^{1/2}\mathbf{v}_{ti}$
gyroradii	$\rho_i = \sqrt{2}\,\mathbf{v}_{ti}/(Z_i eB/m_i c)$ $\rho_s = \rho_i \tau^{1/2}$
profile scale lengths	$L_a = a \,/\, \nabla a$, $\varepsilon_a = L_a/R$
	$\eta_i = L_{n_e}/L_{T_i}$
magnetic shear	$\hat{s} = \varepsilon R q/\nabla q$
shear length	$L_s = Rq/\hat{s}$
collision frequencies	$\nu_{ei} = 2.9 \bullet 10^{-12}\, n_e\, Z_{eff}\, \Lambda_C\, T_e^{-3/2}$
	$\nu_{ii} = 4.8 \bullet 10^{-14}\, n_i\, Z_i^4\, \Lambda_C\, m_i^{-1/2}\, T_i^{-3/2}$
	$\Lambda_C = 31 - 0.5 \log(n_e) + \log(T_e)$
mode frequency	ω
bounce frequency (species j)	$\omega_{bj} = \varepsilon^{1/2}\mathbf{v}_{tj}/qR$
magnetic drift frequency	$\omega_{di} = k_\theta \rho_i \mathbf{v}_{ti}/R$
transit frequency (species j)	$\omega_{tj} = \mathbf{v}_{tj}/qR$
diamagnetic frequencies	$\omega_{*i} = k_\theta \rho_i \mathbf{v}_{ti}/L_n$, $\omega_{*e} = k_\theta \rho_s c_s/L_n$
collisionality parameter	$\nu_{*j} = \nu_{ji} \,/\, (\varepsilon \omega_{bj})$
ratio thermal/magnetic pressure	$\beta = 2\mu_o p/B$

References

[1] Liewer P., *Nucl.Fus.* **25** (1985) 543

[2] Duechs D.F. *et al.*, in Plasma Physics and Controlled Nuclear Fusion Research 1986 (Proc. 11th Int. Conf., Kyoto), Vol.I, IAEA, Vienna (1987) 325

[3] Tibone F., Corrigan G. and Stringer T.E., *Europhysics Conf. Abstracts* **14B-II** (1990) p.805

[4] Ross D.W. *et al.*, University of Texas Report FRCR-295 (1987)

[5] Mattor N., *Phys.Fluids* **B3** (1991) 2153

[6] Blum J., Lazzaro E., O'Rourke J., Keegan B., Stephan Y., *Nucl.Fus.* **30** (1990) 1475

[7] Stubberfield P.M., Watkins M.L., "Multiple Beam Pencil", JET Report DPA-06 (1987)

[8] Eriksson, L.-G. *et al., Nucl.Fus.* **29** (1989) 87

[9] Chang C., Hinton F.L. *Phys.Fluids* **29** (1986) 3314

[10] The JET Team, in Plasma Physics and Controlled Nuclear Fusion Research 1988 (Proc. 12th Int. Conf., Nice), Vol.I, IAEA, Vienna (1989) 215

[11] The JET Team, *Nucl.Fus.* **32** (1992) 187

[12] Horton W., Choi D., Tang W.M., *Phys.Fluids.* **24** (1981) 1077

[13] Guzdar P.N. *et al., Phys.Fluids* **26** (1983) 673

[14] Horton W., *Phys.Rep.* **192** (1990) 1

[15] Biglari H., Diamond P.H., Rosenbluth M.N., *Phys.Fluids* **B1** (1989) 1980

[16] Romanelli F., *Phys.Fluids* **B1** (1989) 1018

[17] Dominguez R.R., Waltz R.E., *Phys.Fluids* **31** (1988) 3147

[18] Sydora R.D. *et al., Phys.Rev.Lett.* **64** (1990) 2015

[19] Guo S.C. *et al., Plas.Phys.Cont.Fus.* **31** (1989) 423

[20] Hong B.G., Horton W., *Phys.Fluids* **B2** (1990) 979

[21] Dominguez R.R., Waltz R.E., *Nucl.Fus.* **29** (1989) 885

[22] Hong B.G., Choi D., Horton W., *Phys.Fluids* **B2** (1990) 1872

[23] Romanelli F., Briguglio S., *Phys.Fluids* **B2** (1990) 754

[24] Romanelli F., Chen L., Briguglio S., *Phys.Fluids* **B3** (1991) 2496

[25] Kim Y.B. *et al., Phys.Fluids* **B3** (1991) 384

[26] Kadomtsev B.B., Pogutse O.P., *Nucl.Fus.* **11** (1971) 67

[27] Diamond P.H., Biglari H., *Phys.Rev.Lett.* **65** (1990) 2865

[28] Cohen B.I. *et al.*, *Nucl.Fus.* **16** (1976) 971

[29] Biglari H., Diamond P.H., Terry P.W., *Phys.Fluids* **31** (1988) 2644 ; *Phys.Rev.Lett.* **60** (1988) 200

[30] Xu X.Q., Rosenbluth M.N., *Phys.Fluids* **B3** (1991) 1807

[31] Garbet X. *et al.*, *Phys.Fluids* **B4** (1992) 136

[32] Guo S.C. and Romanelli F., *(private communication)*

[33] Beklemishev A.D. and Horton W., *Phys.Fluids* **B4** (1992) 200

Figure 1

Summary of experimental measurements and transport analysis results used to compare with theory for a JET limiter L-mode discharge (# 19699, plasma current 3 MA, toroidal field 2.8 T).

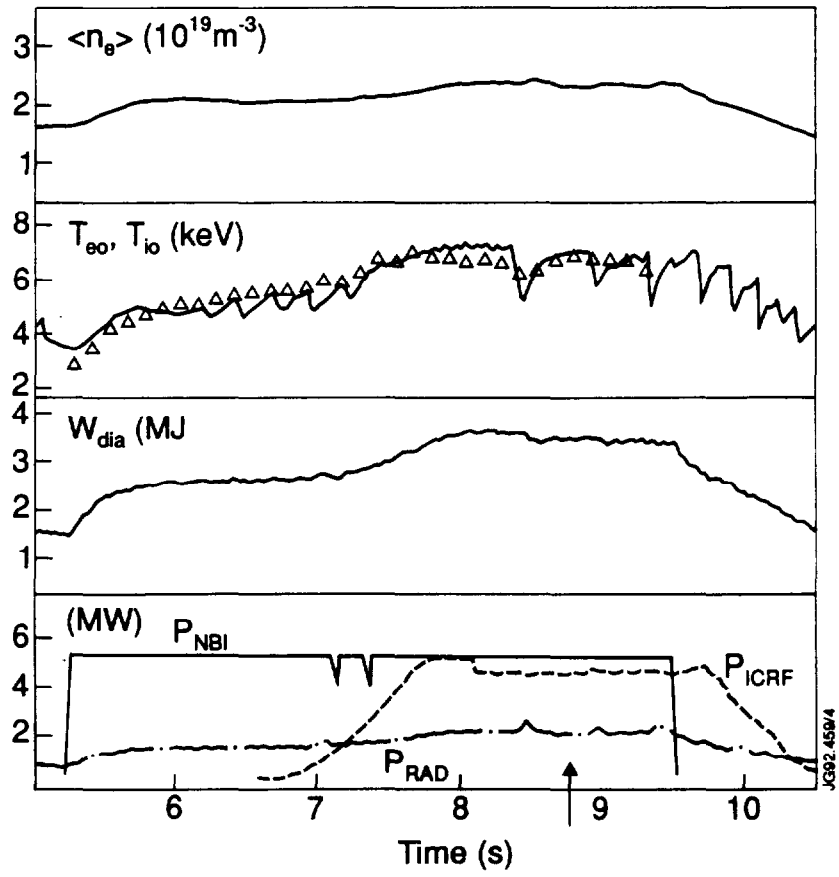

a) time evolution of plasma parameters. From top to bottom, the measured traces represent average electron density, central electron and ion temperature (solid line and open triangles, respectively), total energy content, auxiliary input power and power lost by radiation. The arrow indicates the time at which, in approximate steady-state conditions, local transport analysis has been performed.

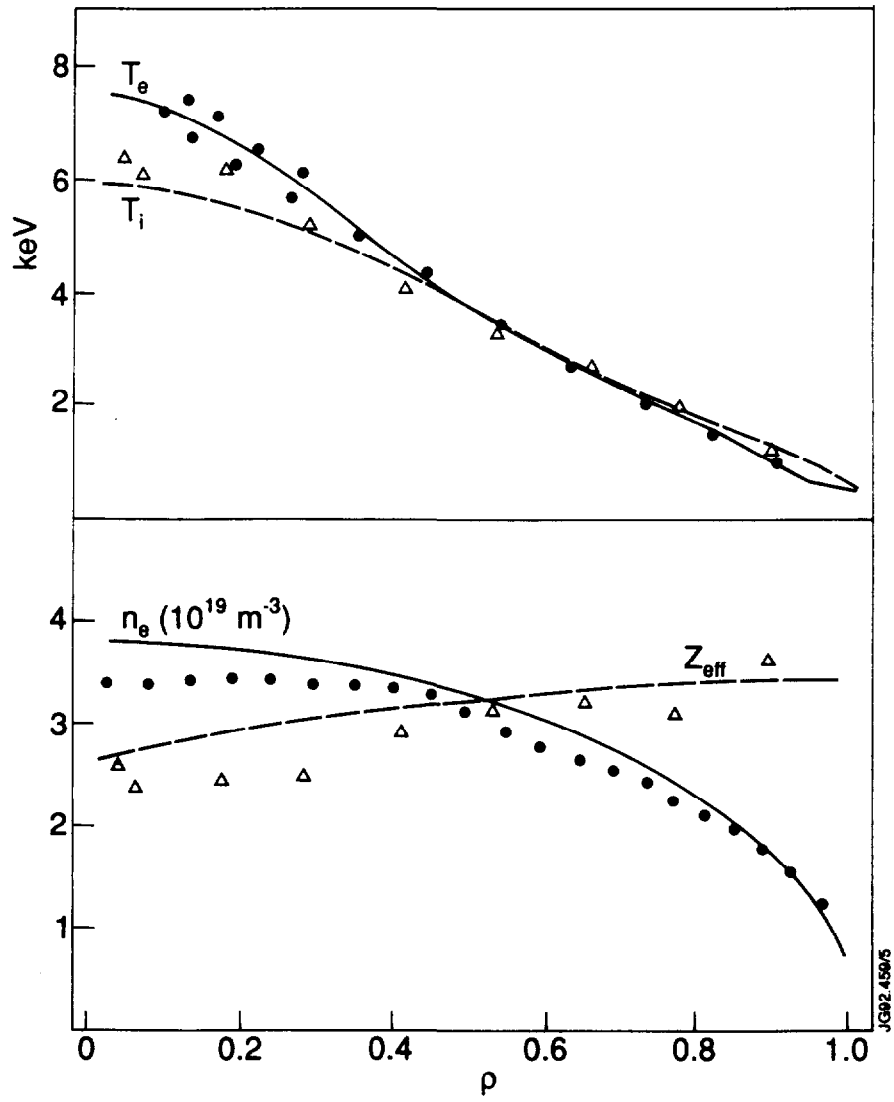

b) measured plasma profiles at time $t \simeq 8.8$ sec in Figure 1a, plotted as a function of flux surface coordinate. The electron temperature data points are from the ECE diagnostic, ion temperature and effective ionic charge are from charge exchange recombination spectroscopy, electron density is from LIDAR Thomson scattering (solid points) and microwave interferometer (solid line).

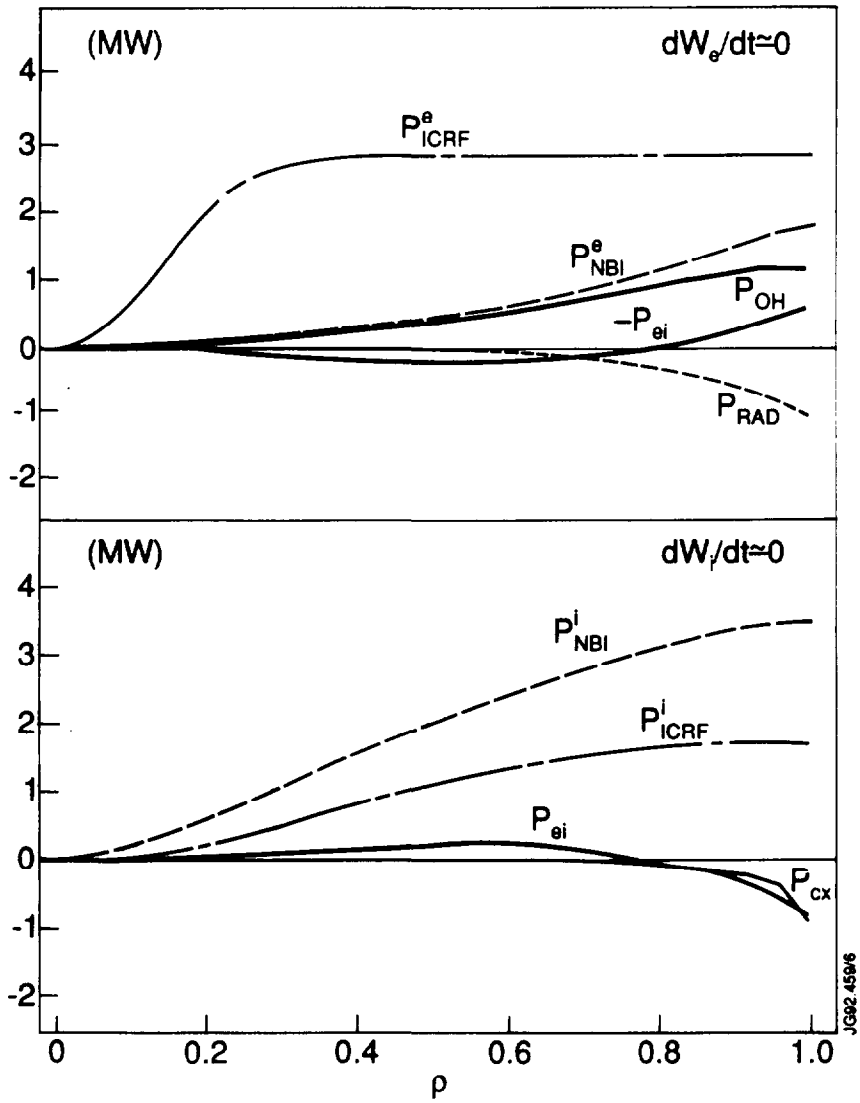

c) local integrated power balances for pulse 19699, for electrons (top) and ions (bottom). The auxiliary power deposition profiles result from calculations with the PION code [8] for ion cyclotron radiofrequency heating (here with He^3 minority in a deuterium plasma) and with the PENCIL code [7] for neutral beam injection heating.

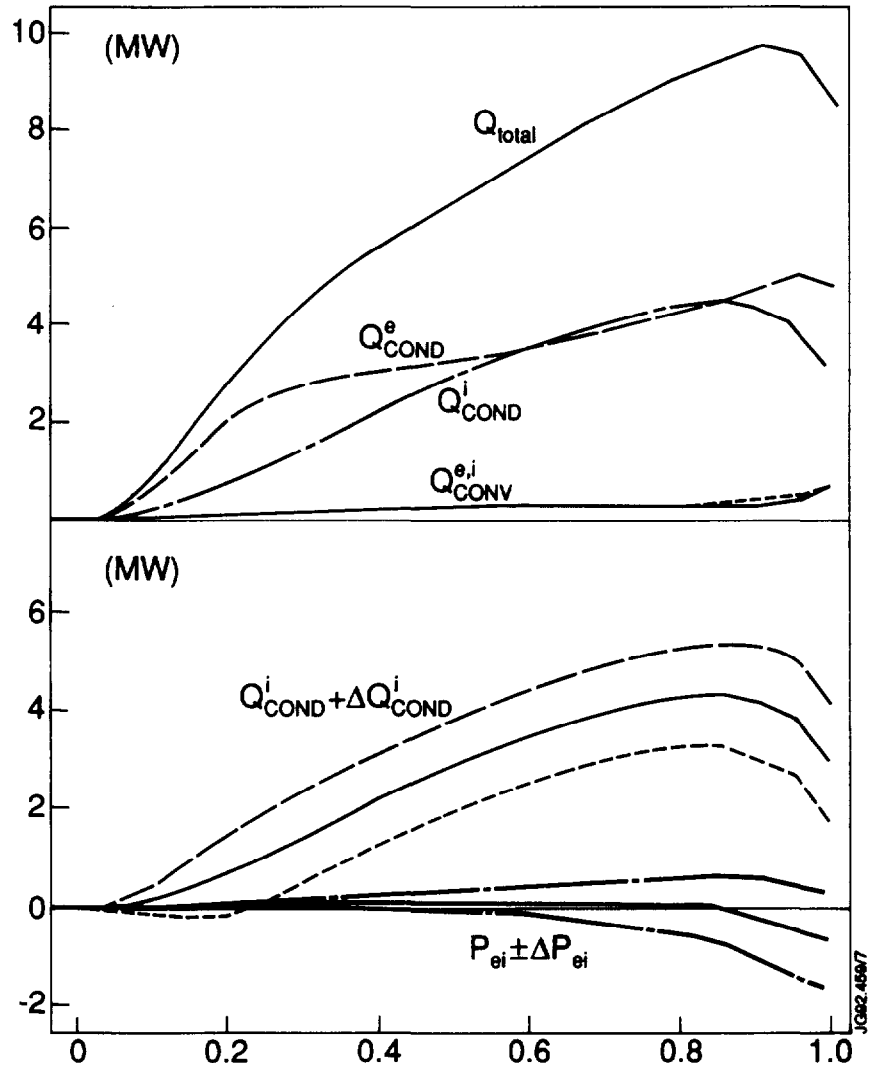

d) splitting of total heat flux inferred from the local power balance into electron and ion heat fluxes (top).
Estimated error on the local ion conductive heat flux, compared with the error on the collisional *e-i* thermal exchange term in the power balance (bottom).

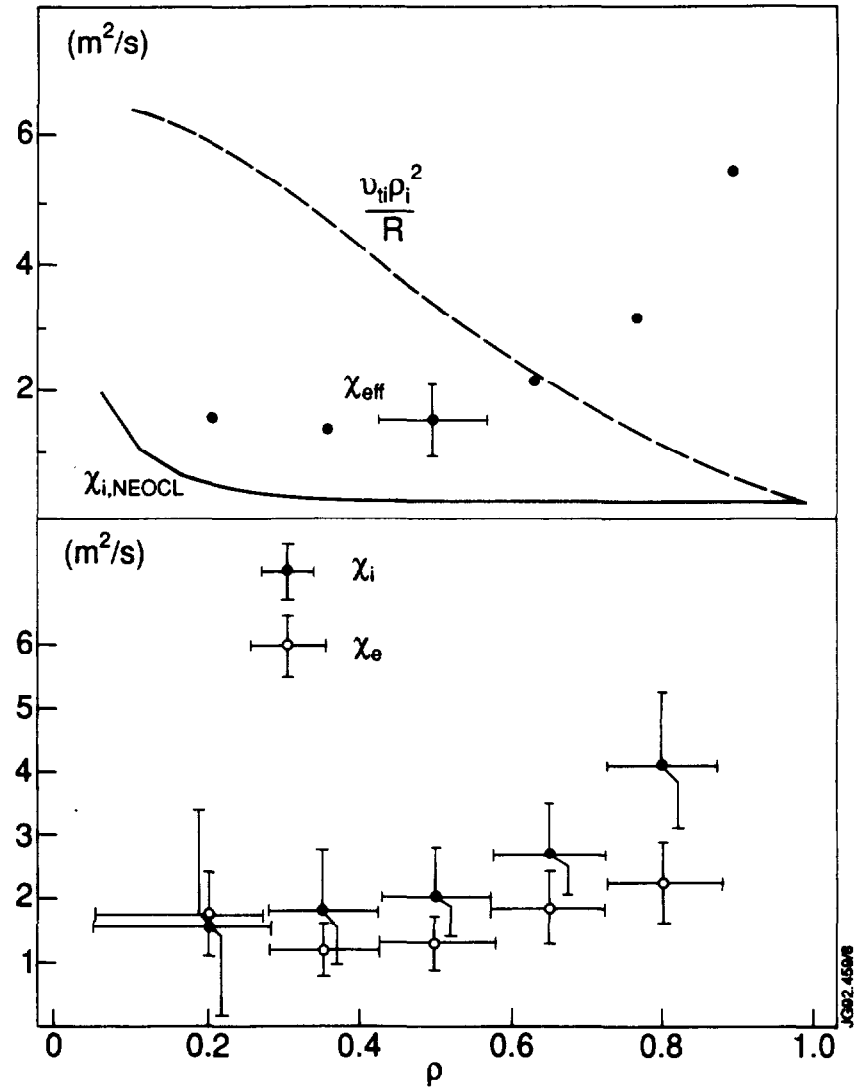

e) "Effective" local thermal conductivity (as defined in the text) compared with the neoclassical value for χ_i, and with the heat diffusion coefficient that constitutes the leading term in most of the models addressed in the paper (top).
Local ion and electron thermal conductivities as inferred from the local power balance (bottom).

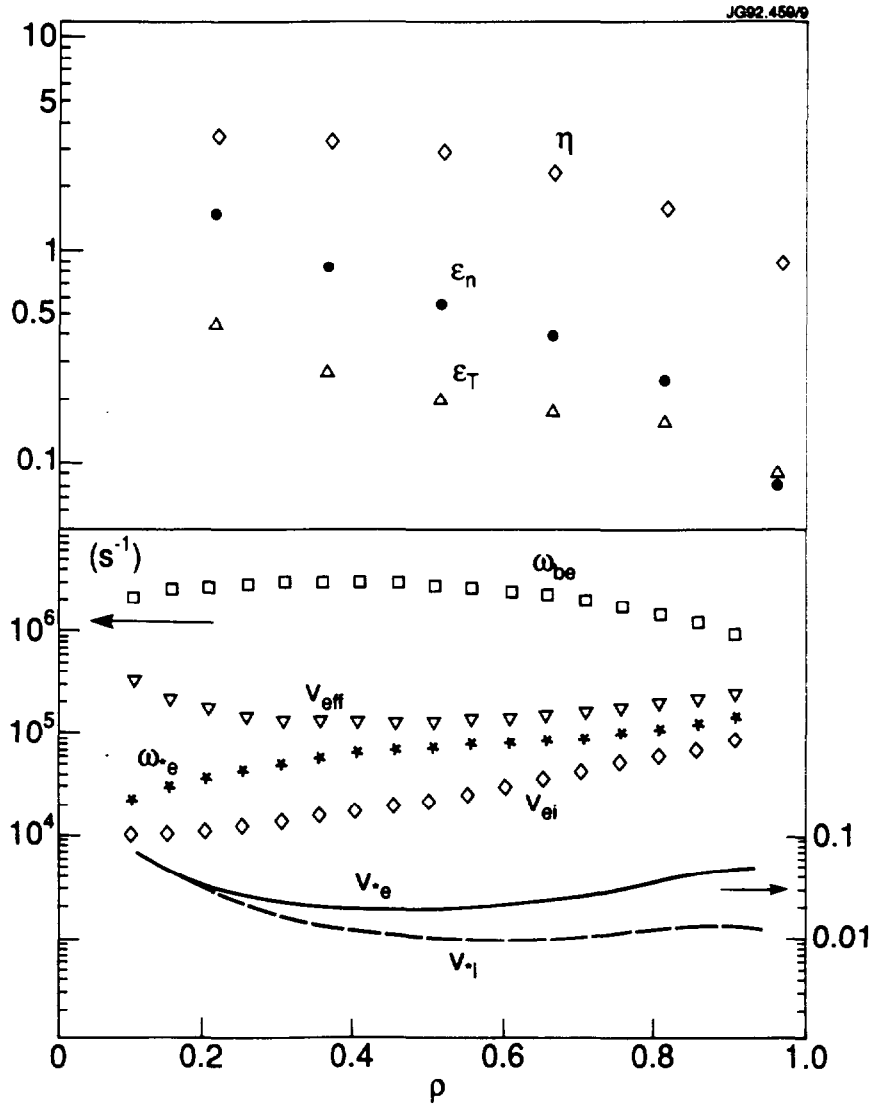

f) profile scale lengths and $\eta_i \equiv L_{n_e}/L_{T_i}$ (top); bounce and diamagnetic frequency and collisionality parameters (bottom) as a function of radius.

Figure 2

Summary of experimental measurements and transport analysis results used to compare with theory for a JET H-mode discharge obtained in the presence of a magnetic separatrix (# 24737, plasma current 3.1 MA, toroidal field 3.0 T).

Parameters in plots **a,b,c,d,e,f** are as in Figure 1. The ion energy flux accounts here for practically the entire observed heat losses; correspondingly, the estimate of error bars on the inferred ion thermal conductivity leads only to a lower bound (and viceversa for the electrons).

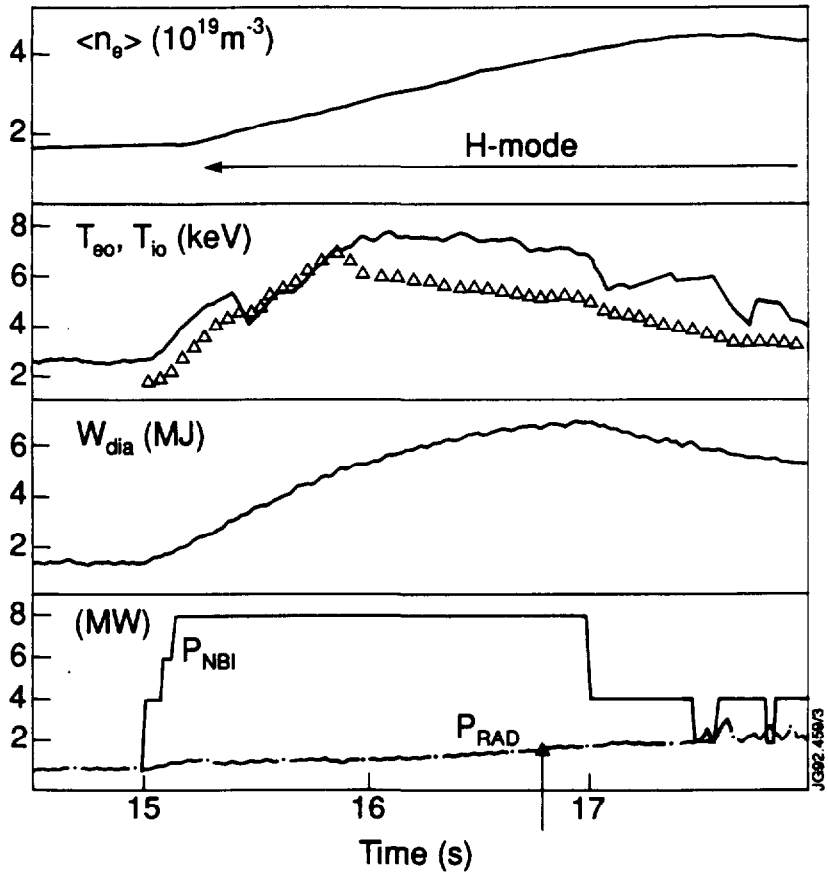

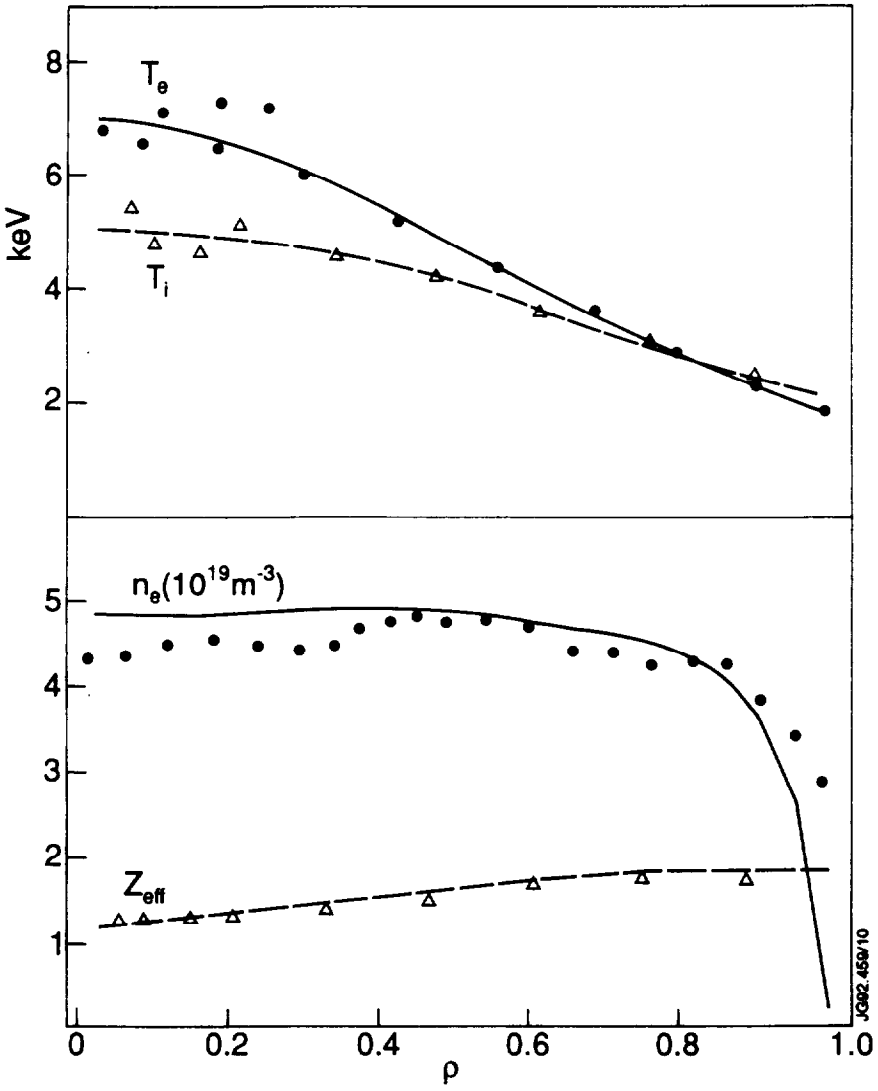
8
6
4
2
keV
T_e
T_i
5
4
3
2
1
$n_e(10^{19}m^{-3})$
Z_{eff}
0
0.2
0.4
0.6
0.8
1.0
ρ
JG92.459/10

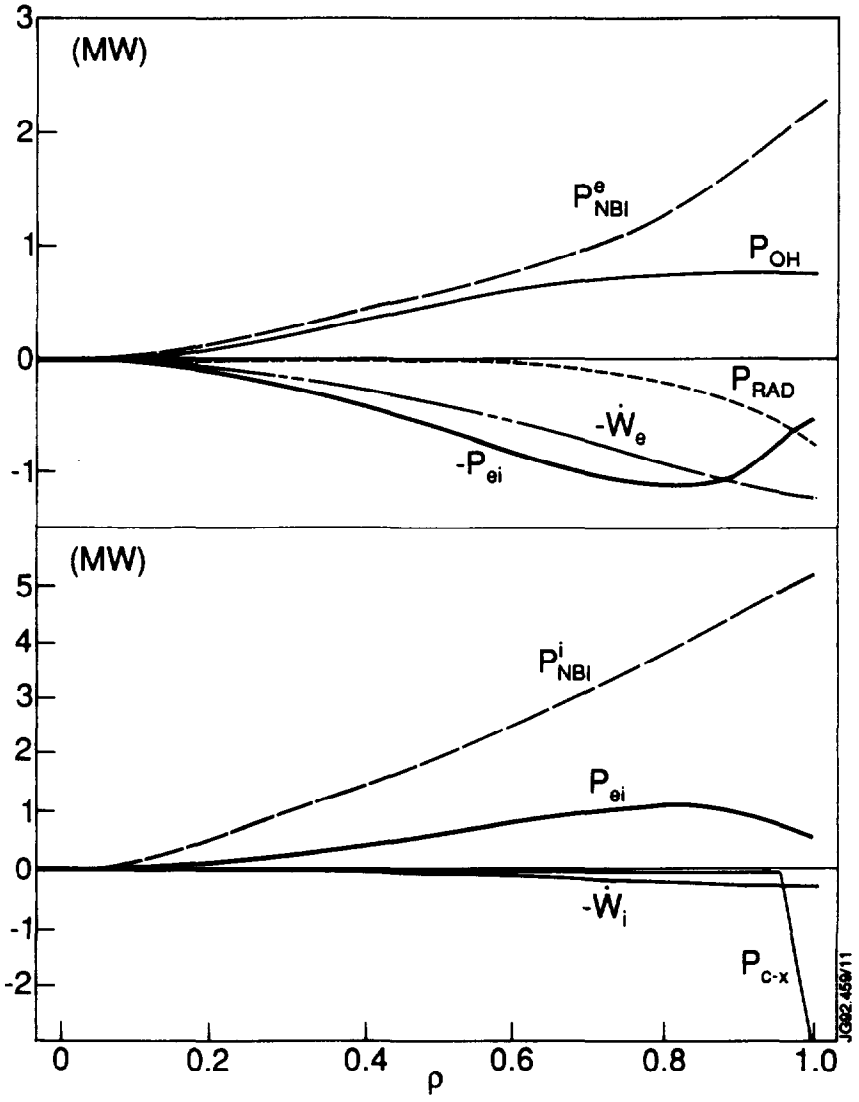
(MW)
3
2
1
0
-1
P^e_{NBI}
P_{OH}
P_{RAD}
$-\dot{W}_e$
$-P_{ei}$
(MW)
5
4
3
2
1
0
-1
-2
P^i_{NBI}
P_{ei}
$-\dot{W}_i$
$P_{c\text{-}x}$
0
0.2
0.4
0.6
0.8
1.0
ρ
JG92.459/11

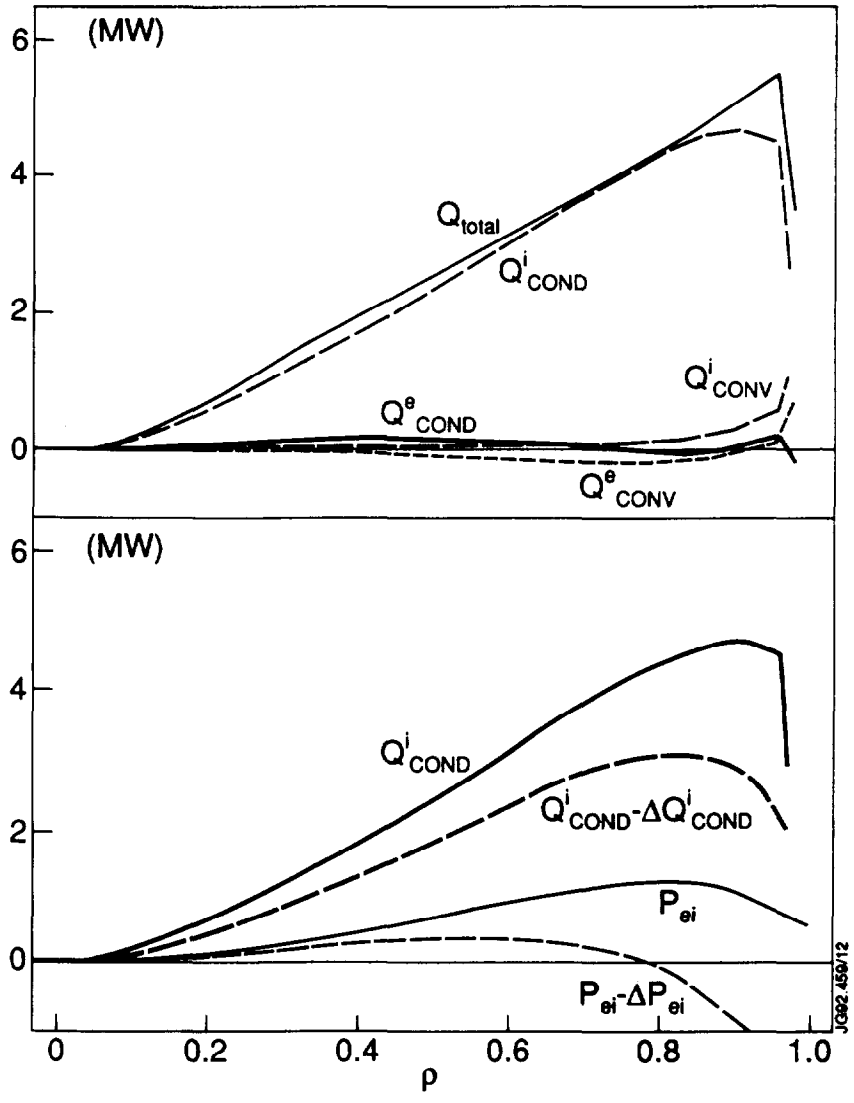
(MW)
6
4
2
0
Q_{total}
Q^i_{COND}
Q^i_{CONV}
Q^e_{COND}
Q^e_{CONV}
(MW)
6
4
2
0
Q^i_{COND}
$Q^i_{COND}-\Delta Q^i_{COND}$
P_{ei}
$P_{ei}-\Delta P_{ei}$
0
0.2
0.4
0.6
0.8
1.0
ρ
JG92.459/12

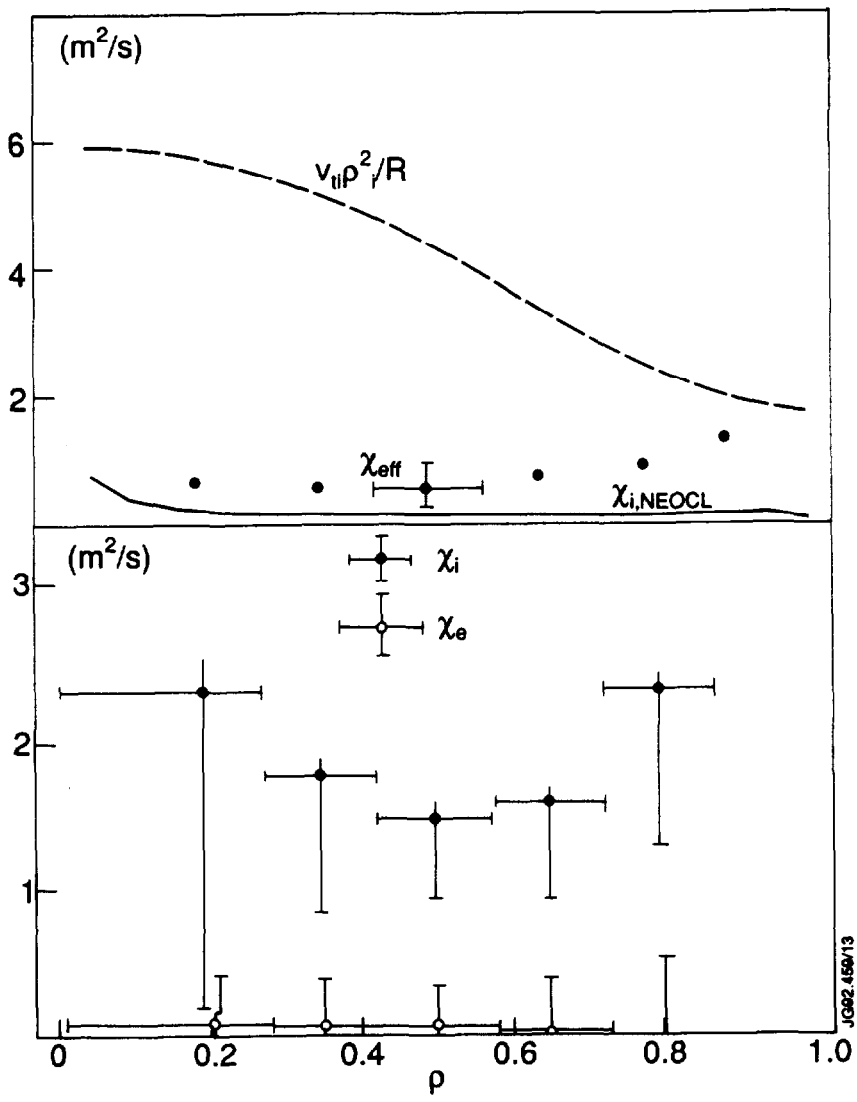
(m²/s)
6
4
2
$v_{ti}\rho^2_i/R$
χ_{eff}
$\chi_{i,NEOCL}$
(m²/s)
3
2
1
χ_i
χ_e
0
0.2
0.4
0.6
0.8
1.0
ρ
JG92.459/13

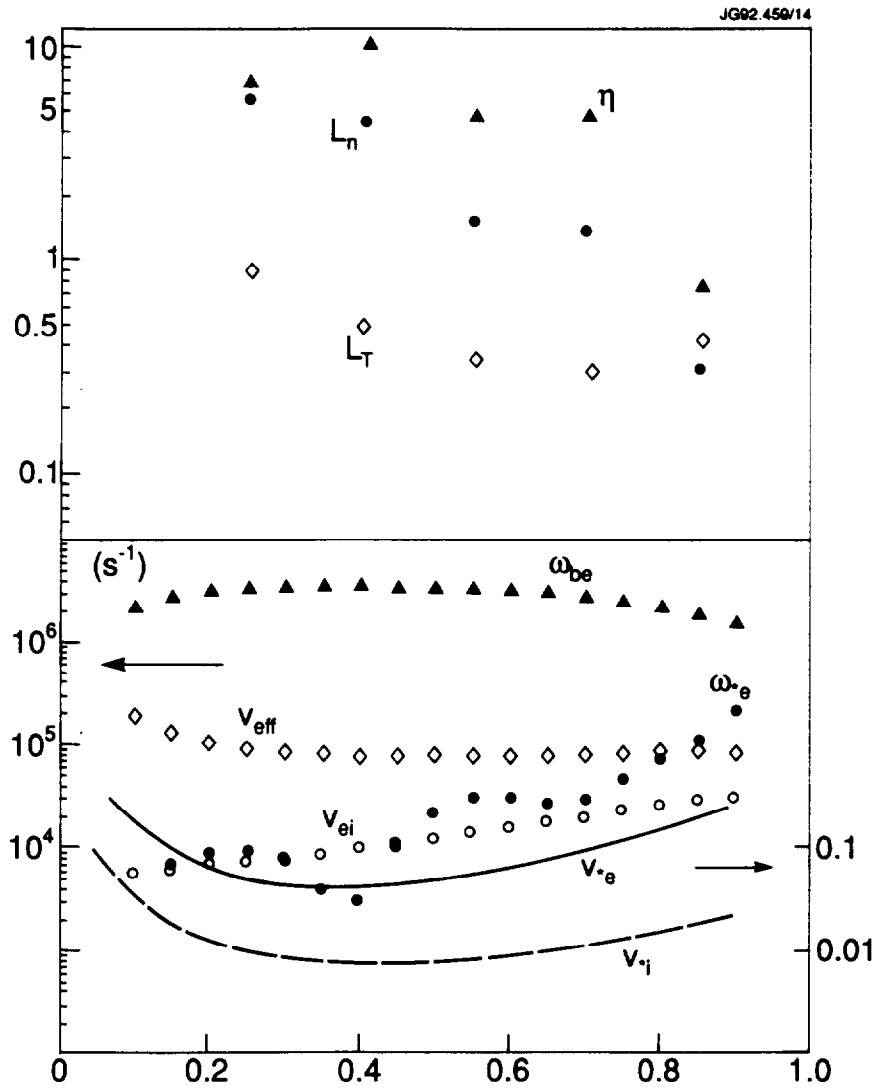
JG92.459/14
10
5
1
0.5
0.1
L_n
L_T
η
(s^{-1})
ω_{be}
10^6
10^5
10^4
ω_{*e}
ν_{eff}
ν_{ei}
ν_{*e}
ν_{*i}
0.1
0.01
0
0.2
0.4
0.6
0.8
1.0

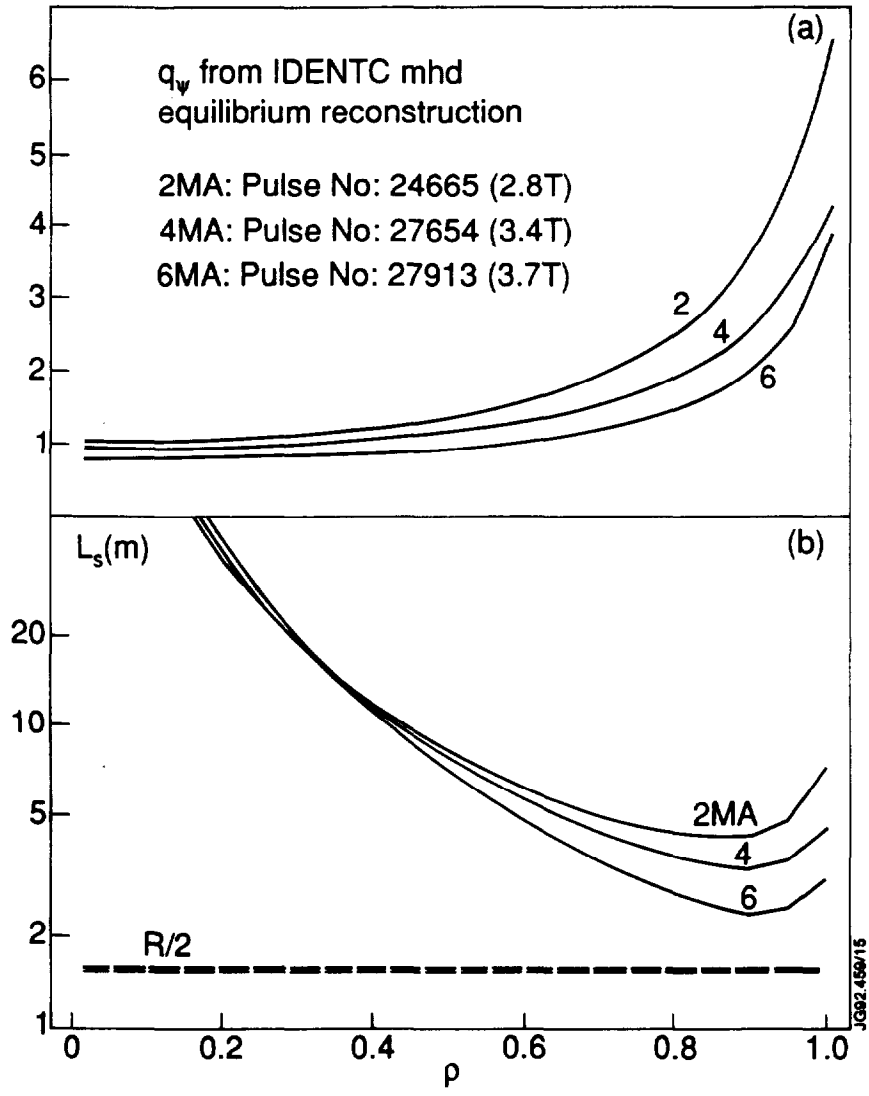

Figure 3

Radial profiles of the inverse rotational transform q_ψ for JET limiter discharges at different values of the plasma current (**a**) and corresponding radial variation of the shear length $L_s \equiv qR/\nabla q$ (**b**).

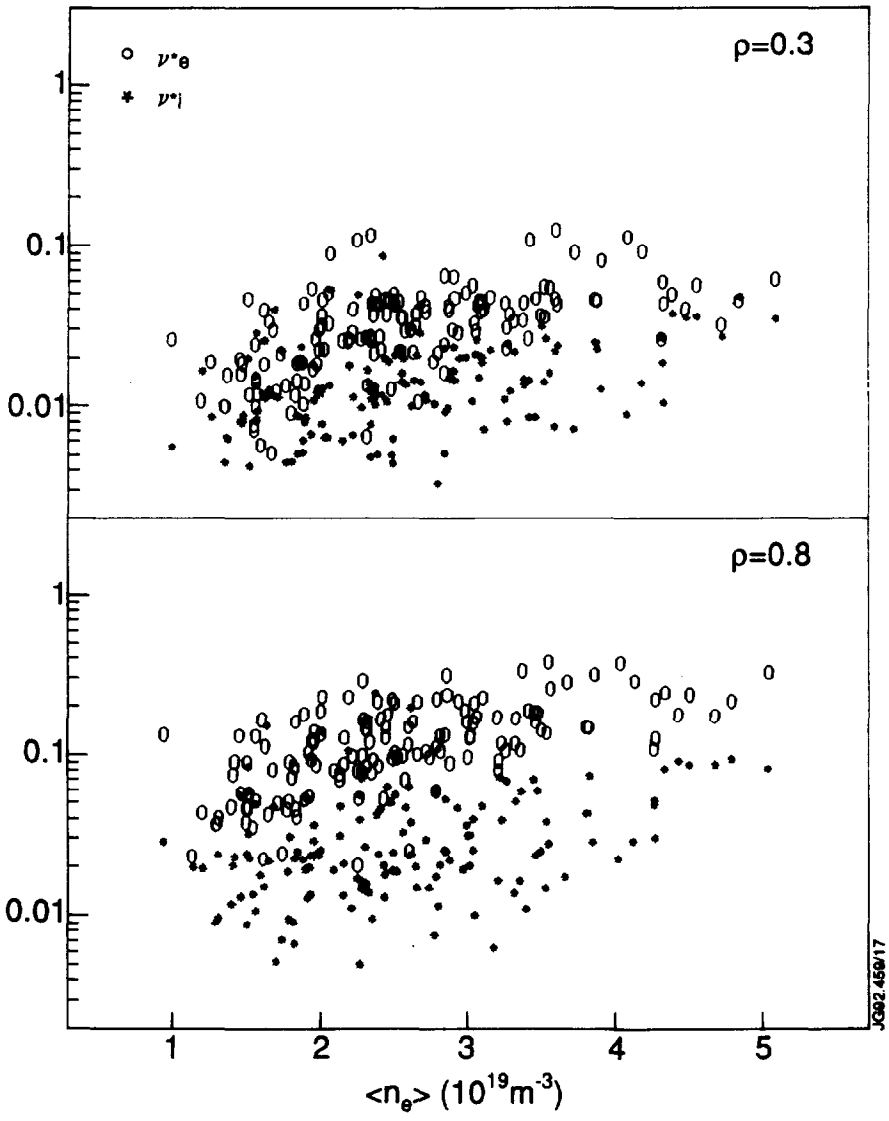

Figure 4

Variation of electron and ion collisionality parameters ν_{*_e} and ν_{*_i} as a function of average plasma density, at two different radial positions. The set of JET data used corresponds to sawtooth-free plasmas with auxiliary heating, at different values of magnetic field and plasma current, and includes both L-mode and H-mode discharges.

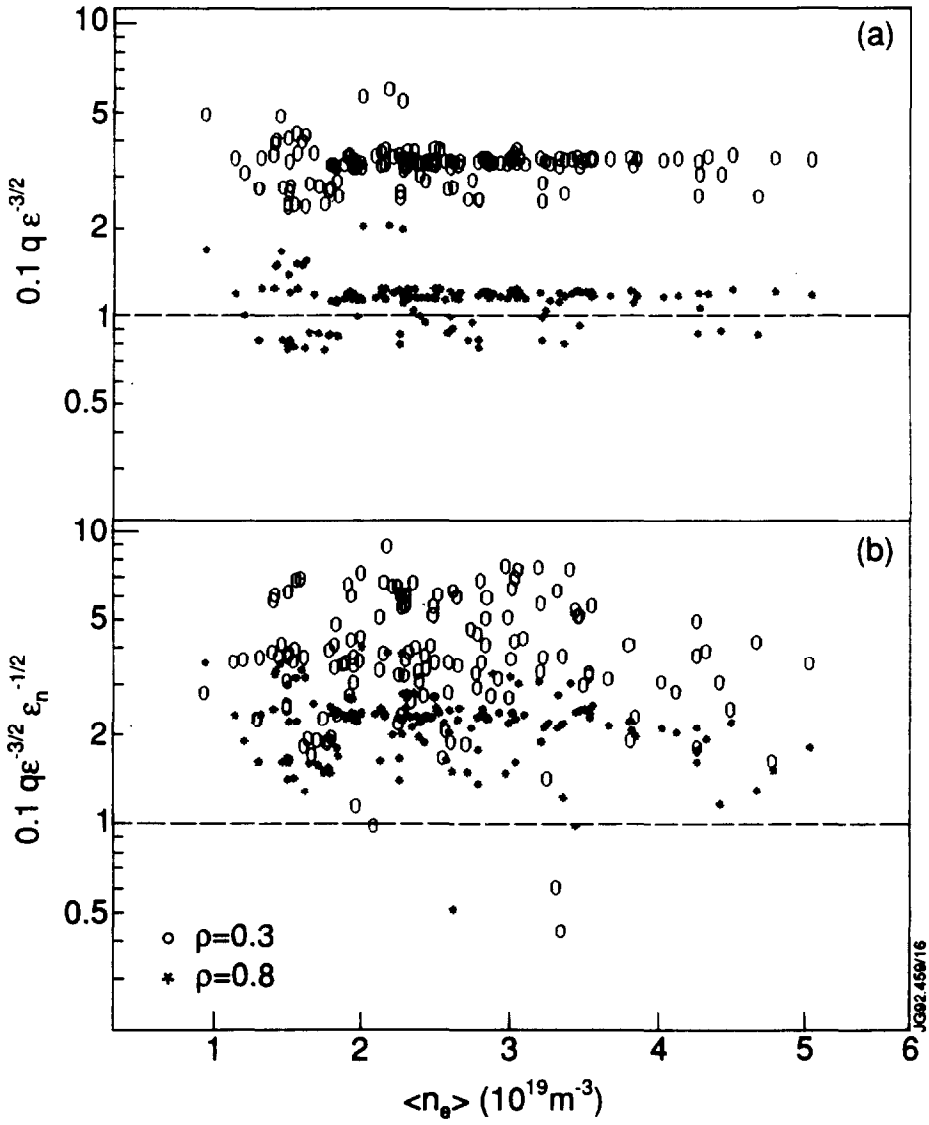

Figure 5

Check of the experimental applicability of the orderings adopted by Biglari et al. [15] (**a**) and by Romanelli [16] (**b**). The data set used is the same as in Figure 4, with $\nu_{*e}, \nu_{*i} < 1$ at both radial positions; $k_\theta \rho_i = 0.1$ has been assumed here. The constraints in Eq.(1) and Eq.(10) are therefore satisfied even for long wavelength modes.

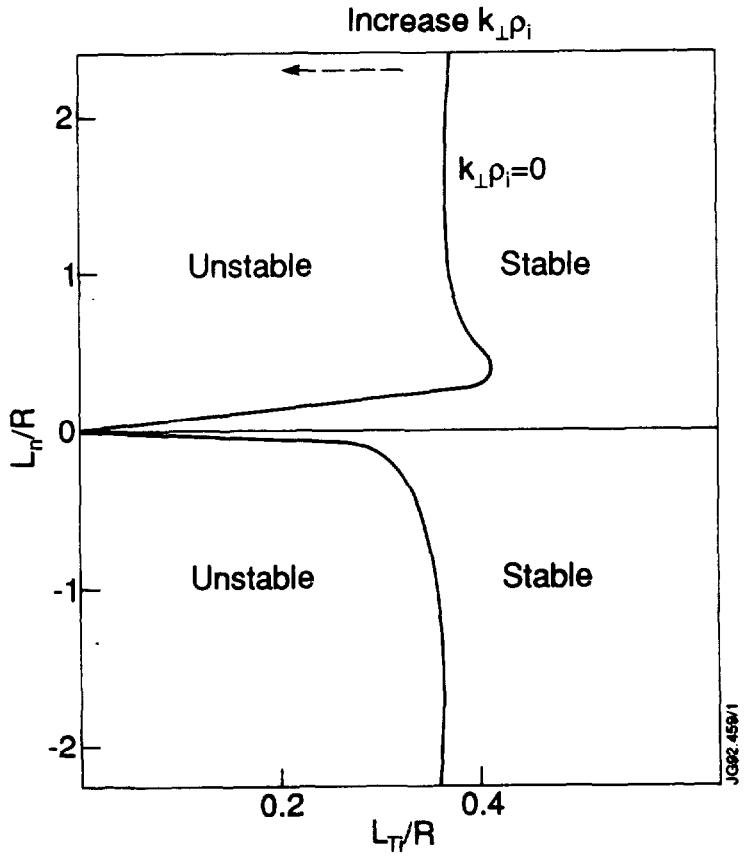

Figure 6

Stability boundaries in the $(\varepsilon_n, \varepsilon_T)$ plane as obtained by Biglari et al. [15] in the limit $k_\perp \rho_i = 0$.

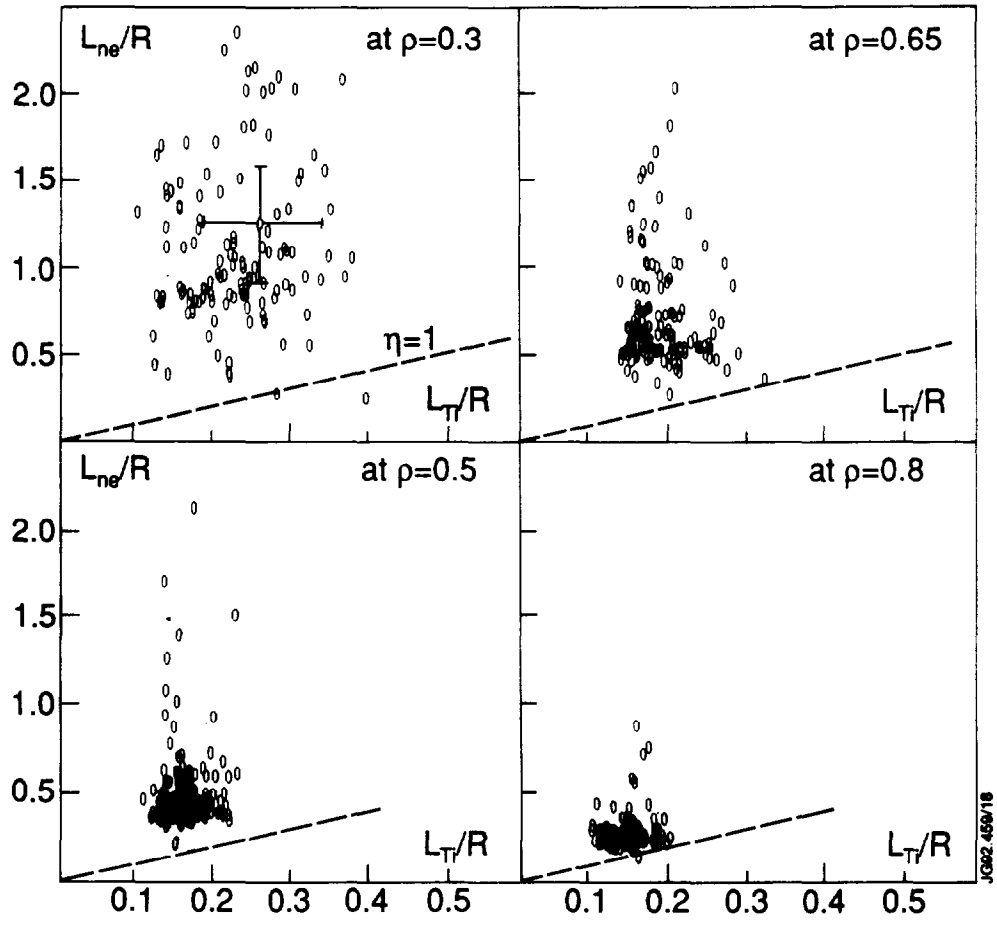

Figure 7

JET experimental data for sawtooth-free discharges (as in Figure 4) with monotonic density profiles, plotted in the stability diagram of Figure 6 for different radial locations across the plasma column. The line $\eta \equiv L_{n_e}/L_{T_i} = 1$ is also drawn for reference.

Figure 8

Comparison of the theoretical ion thermal conductivity of Biglari et al. Eq.(5) with the transport coefficient inferred from the measurements for:

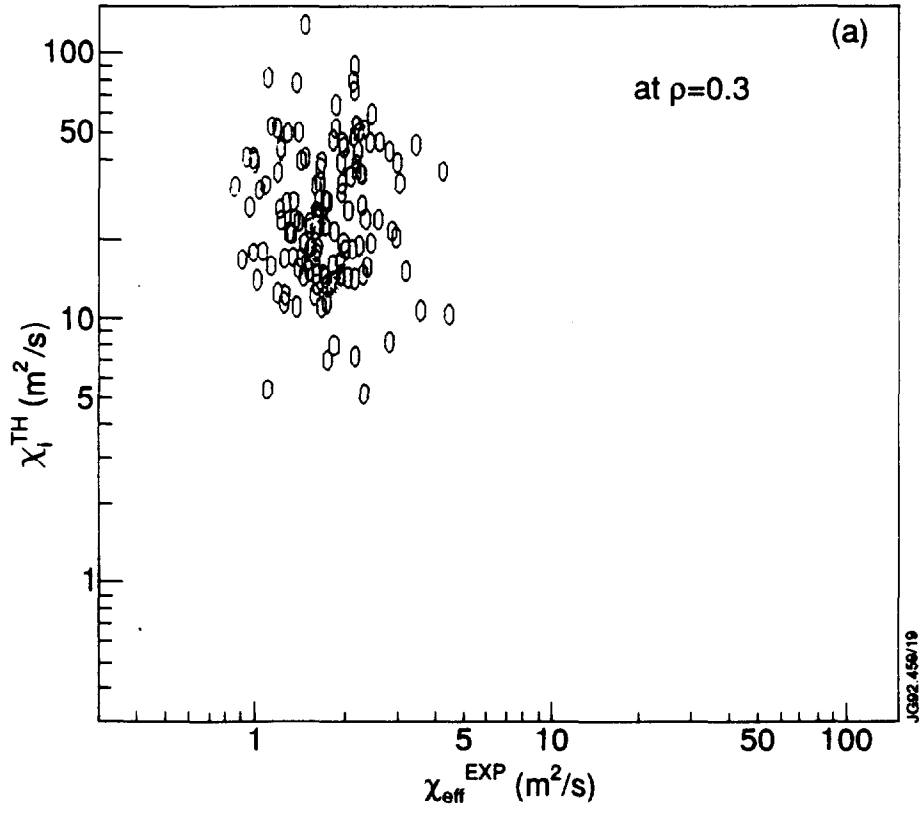

a) the core plasma region of sawtooth-free discharges (same data set as in Figure 4);

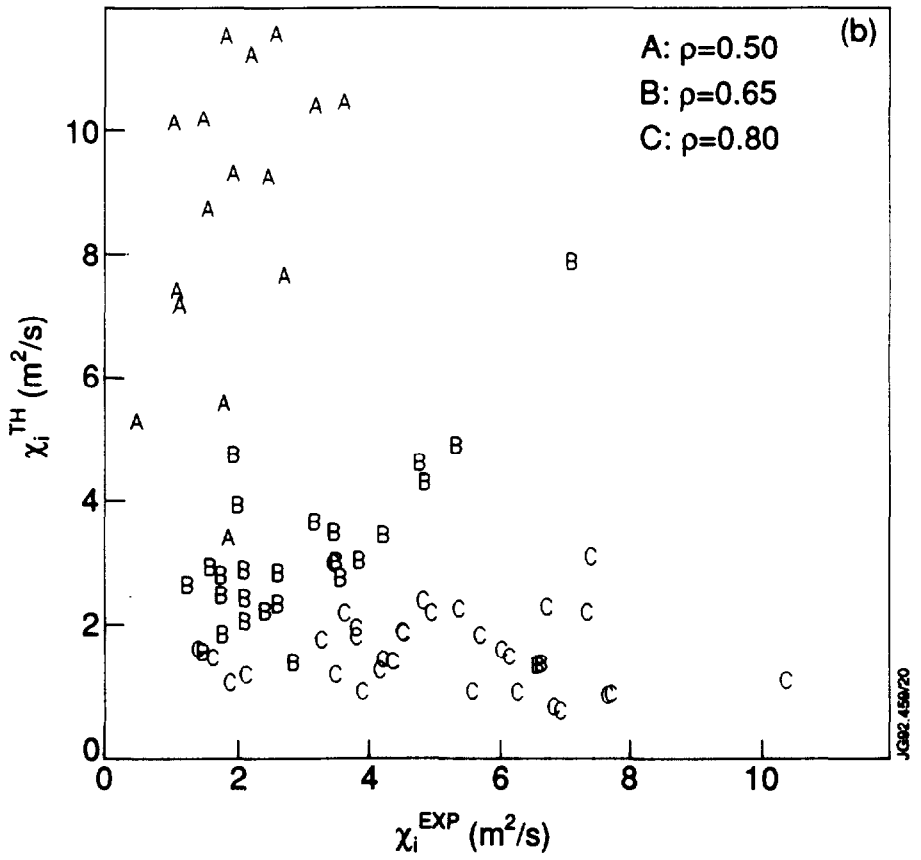

b) the region outside the $q = 1$ surface of plasmas for which a reliable measurement of χ_i is available, and the theoretical constraints Eqs(2,3) are also satisfied.

Figure 9

Comparison of the theoretical ion thermal conductivity of Guo et al. Eq.(6) with the transport coefficient inferred from the measurements for:

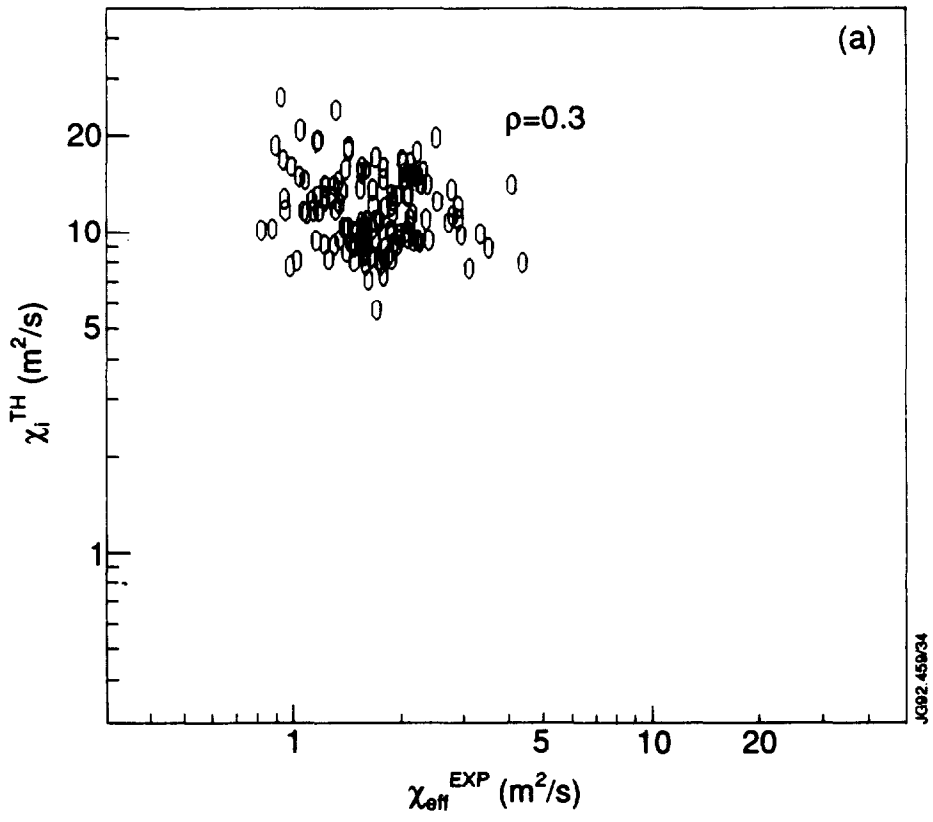

a) the core plasma region of sawtooth-free discharges with flat density profile (subset of the data in Figure 4 having $\varepsilon_n > 1$);

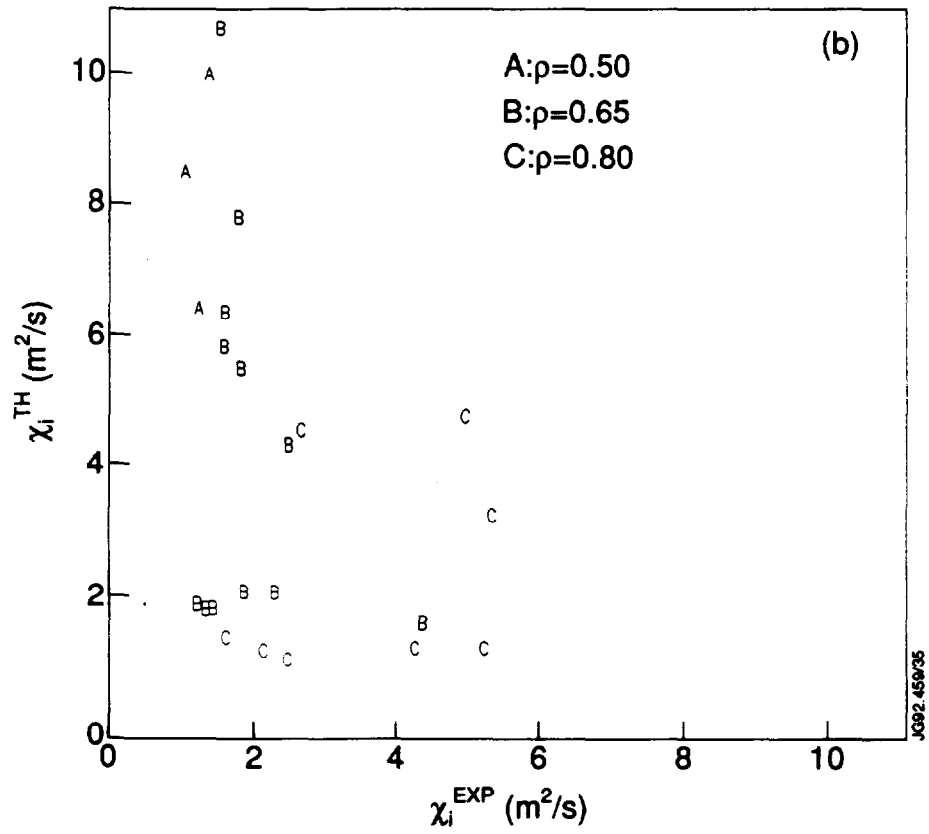

b) the region outside the $q = 1$ surface of plasmas for which a reliable measurement of χ_i is available and $\varepsilon_n > 1$.

Figure 10

Comparison of the theoretical ion thermal conductivity of Hong and Horton Eq.(7) with the transport coefficient inferred from the measurements for:

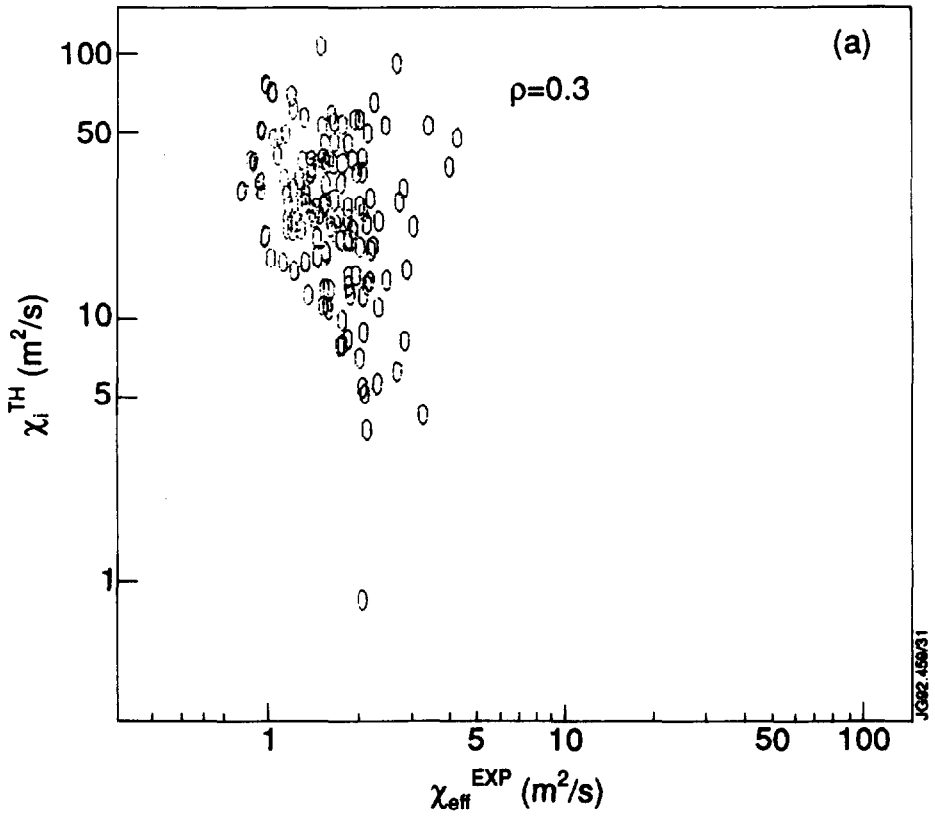

a) the core plasma region of sawtooth-free discharges (same data set as in Figure 4);

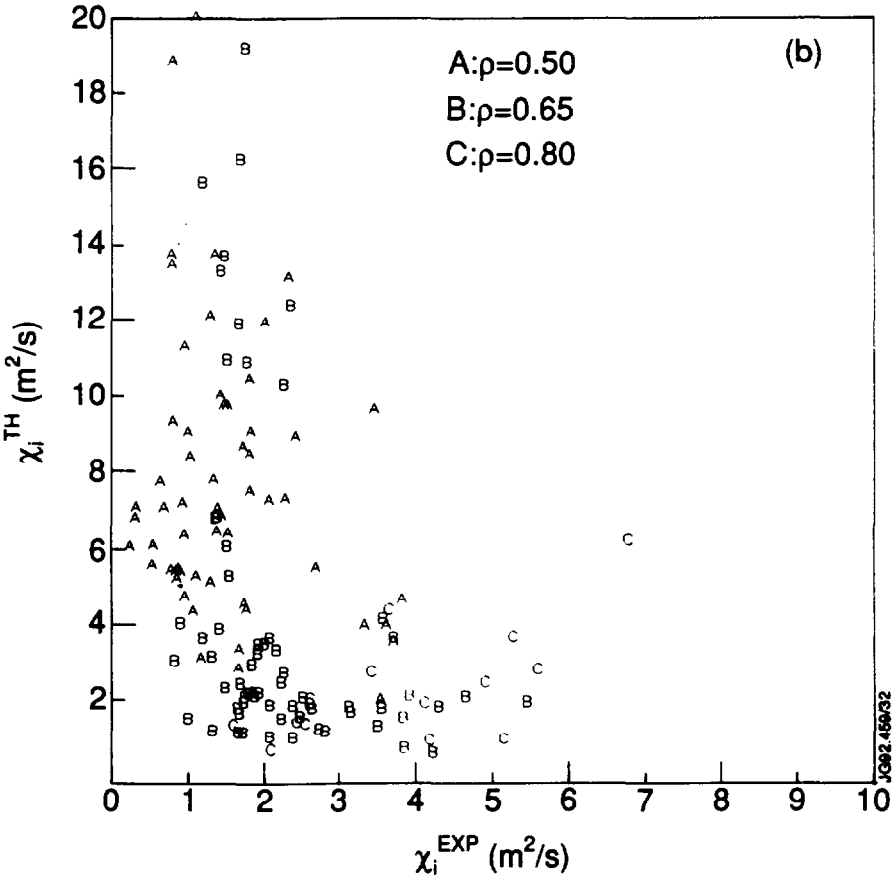

b) the region with $q > 1$ of plasmas for which χ_i can be inferred from the experimental data with uncertainty $< \pm 50\%$.

Figure 11

Comparison of the theoretical ion thermal conductivity of Dominguez and Waltz Eq.(8) with the transport coefficient inferred from the measurements for:

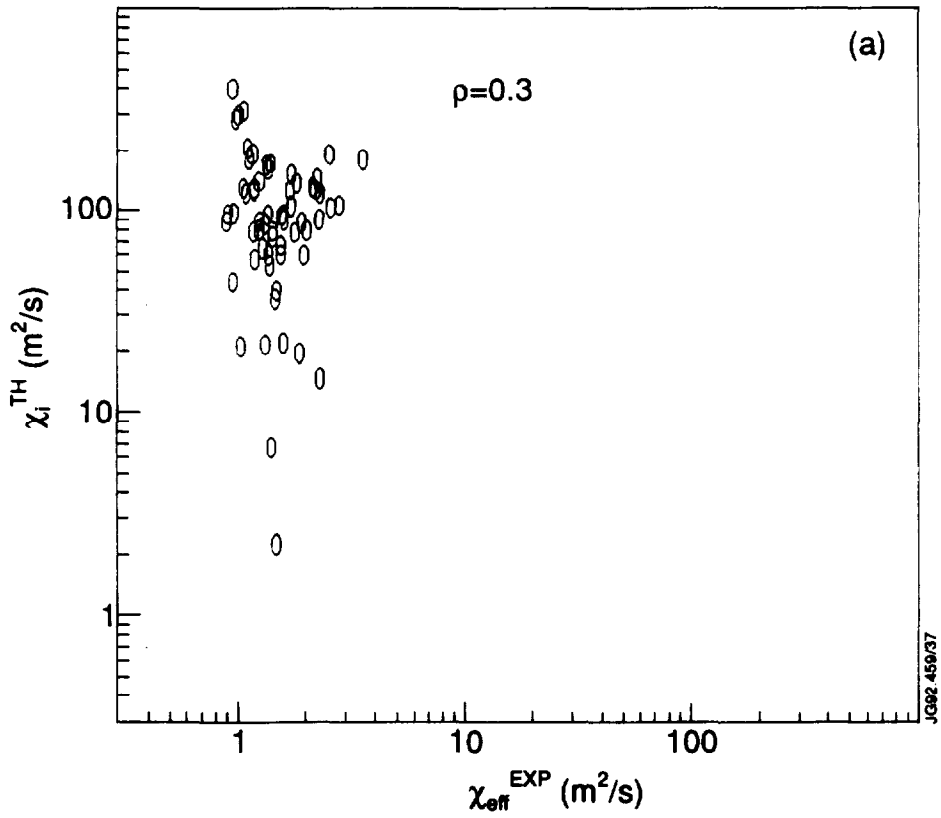

a) the core plasma region of sawtooth-free discharges having $\varepsilon_T < 0.25$ (subset of the data in Figure 4);

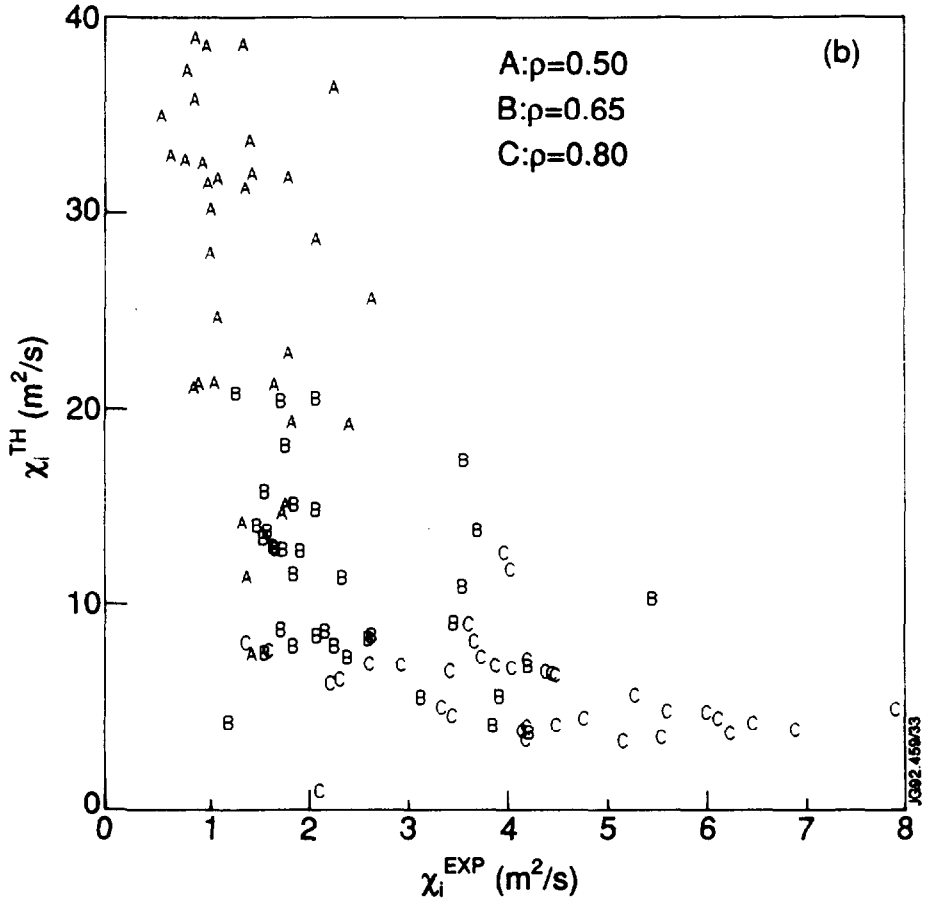

b) the "confinement region" of plasmas for which a reliable measurement of χ_i is available.

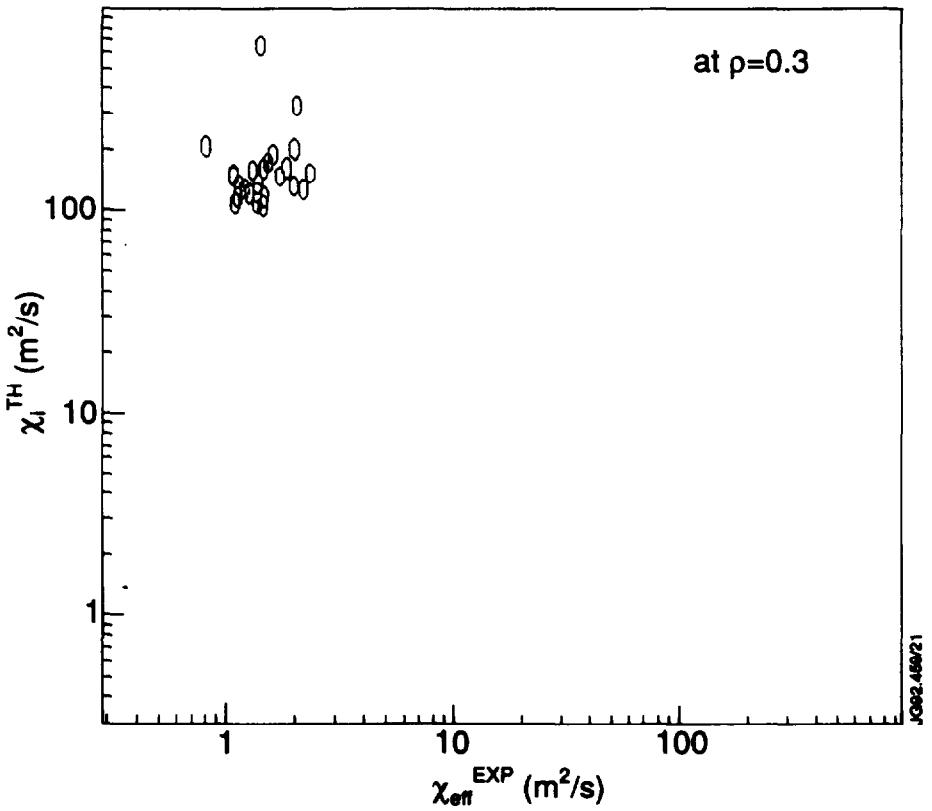

Figure 12

Comparison of the theoretical ion thermal conductivity of Hong et al. Eq.(9) with the transport coefficient inferred from the measurements. Only a few experimental data points from the plasma core have sufficiently low shear and sufficiently high density peaking to make the model applicable.

Figure 13

Comparison of the theoretical ion thermal conductivity of Romanelli Eq.(12) with the transport coefficient inferred from the measurements for:

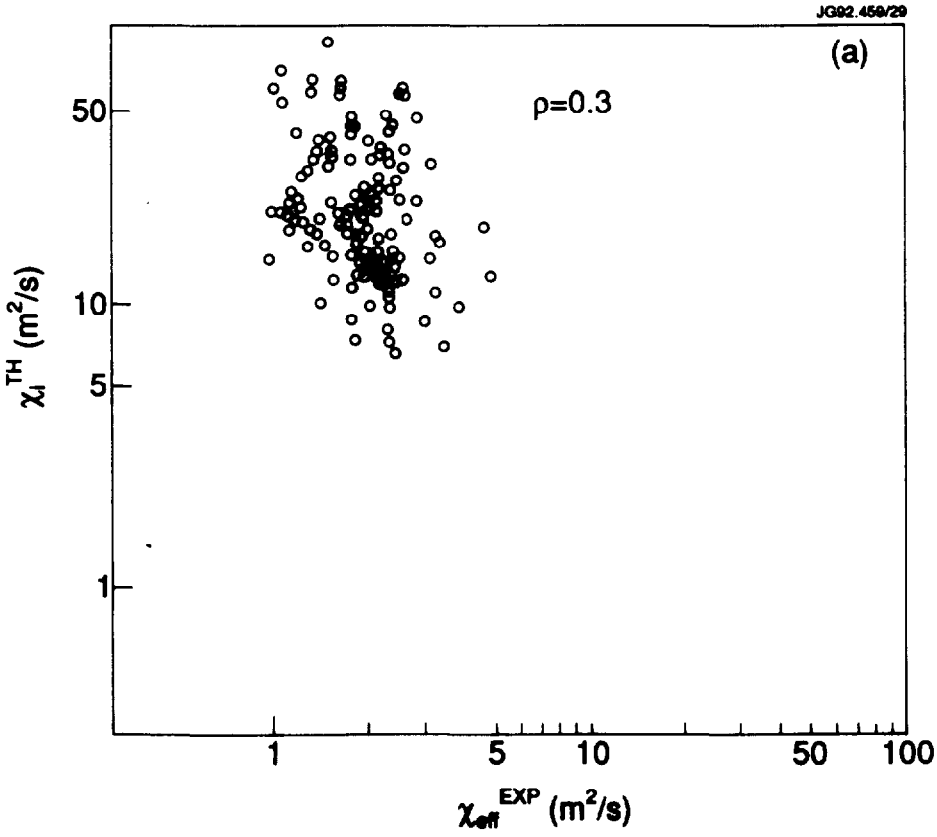

a) the core plasma region of sawtooth-free discharges (same data set as in Figure 4);

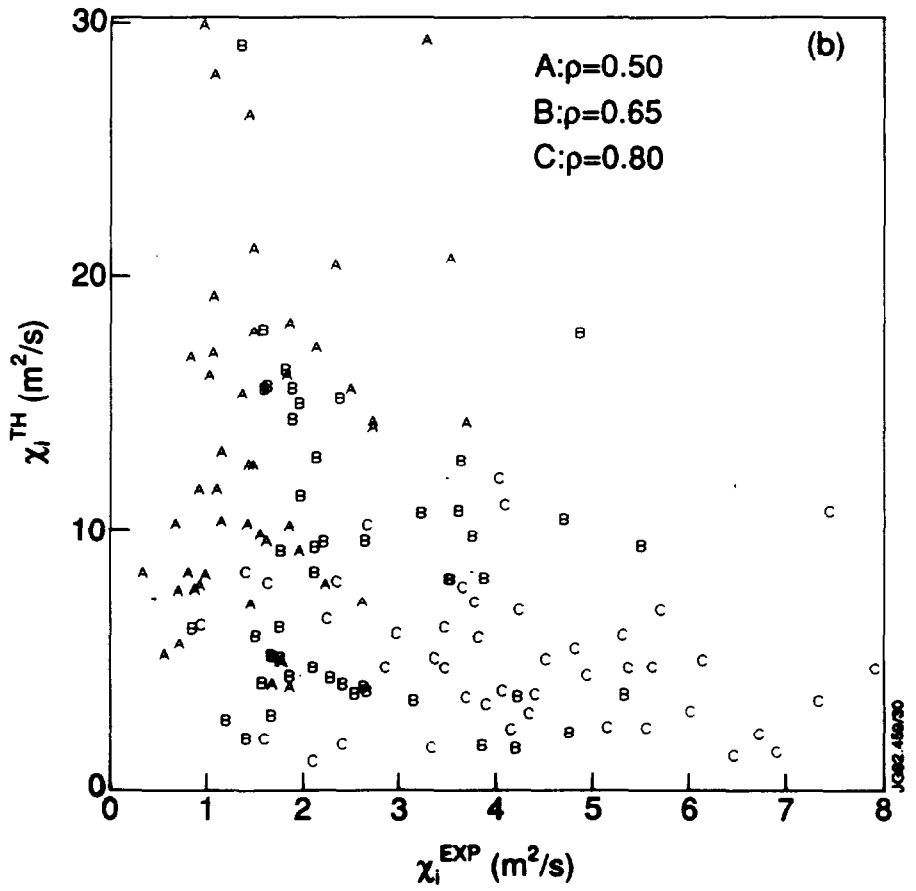

b) the region with $q > 1$ of plasmas for which χ_i can be inferred from the experimental data with uncertainty $< \pm 50\%$.

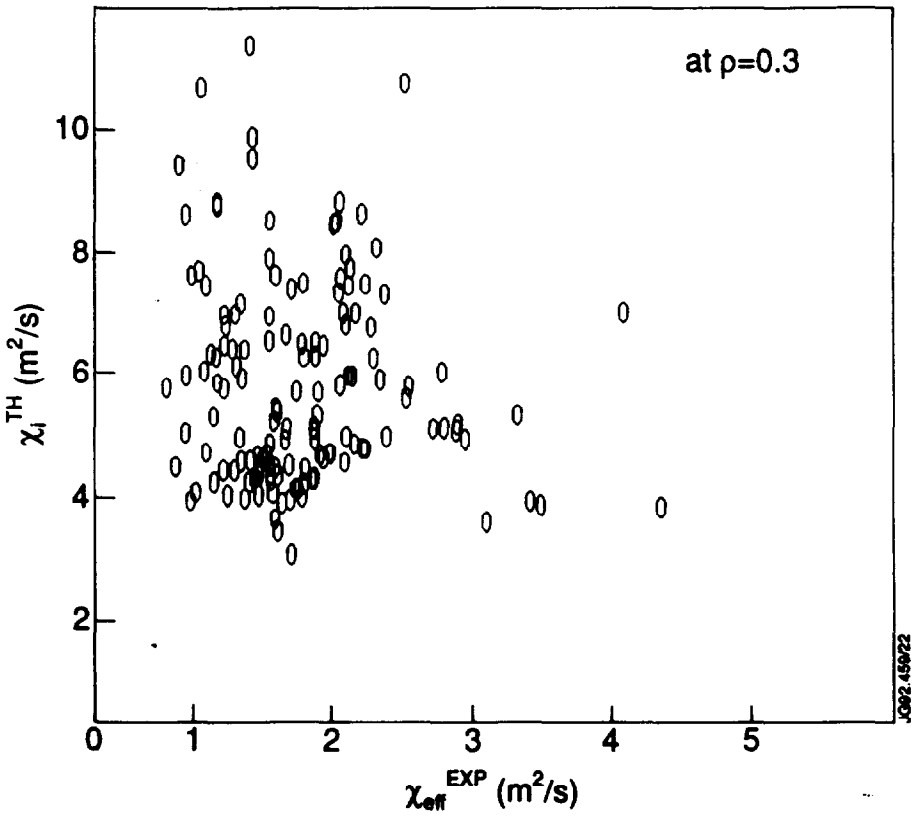

Figure 14

Comparison of the theoretical ion thermal conductivity of Romanelli, Chen and Briguglio Eq.(17) with the measured "effective" transport coefficient for the data points (a subset of those in Figure 4) for which the constraints Eqs(15,16) can be satisfied.

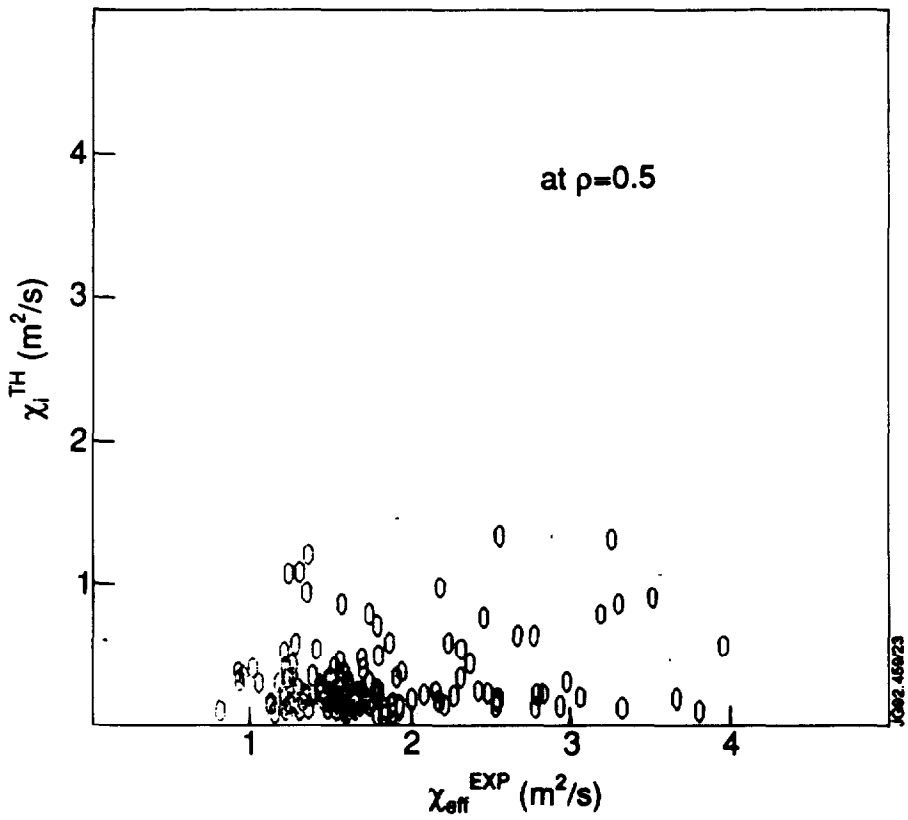

Figure 15

Comparison of the theoretical ion thermal conductivity of Kim et al. Eq.(19) with the measured "effective" transport coefficient for JET sawtooth-free plasmas with flat density profiles ($\varepsilon_n \gtrsim 1$), at a radial position where the constraint Eq.(19) is satisfied.

Figure 17

Comparison of the ion thermal conductivity of Diamond and Biglari's collisionless trapped ion theory Eq.(20) with the transport coefficient inferred from the measurements for:

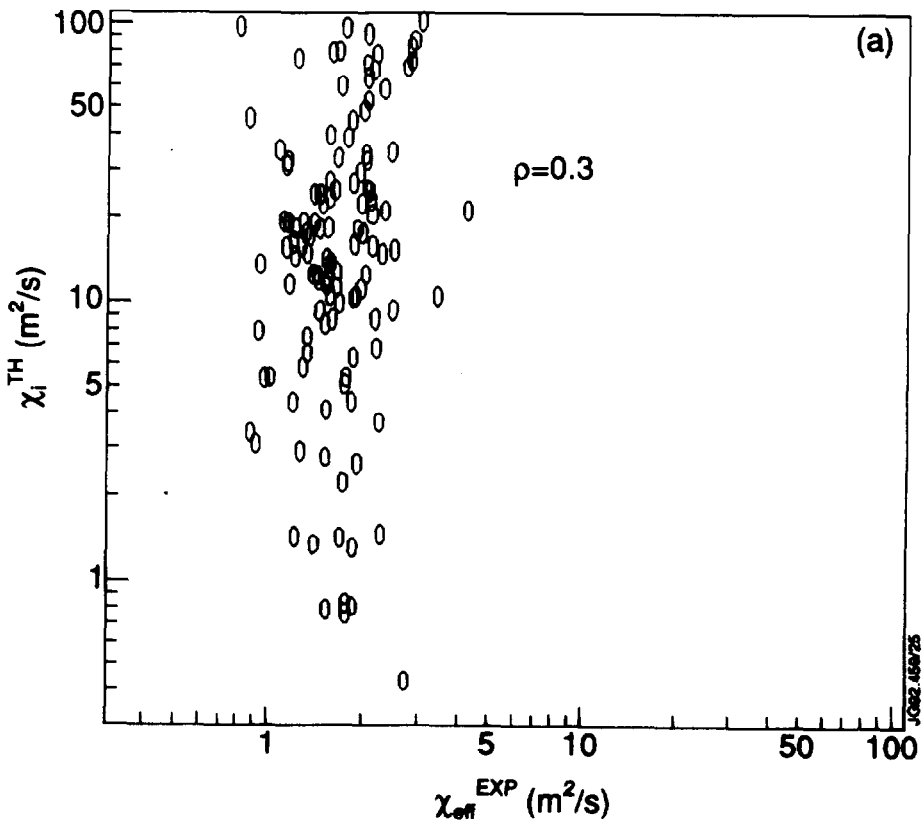

a) the core plasma region of sawtooth-free discharges (same data set as in Figure 4);

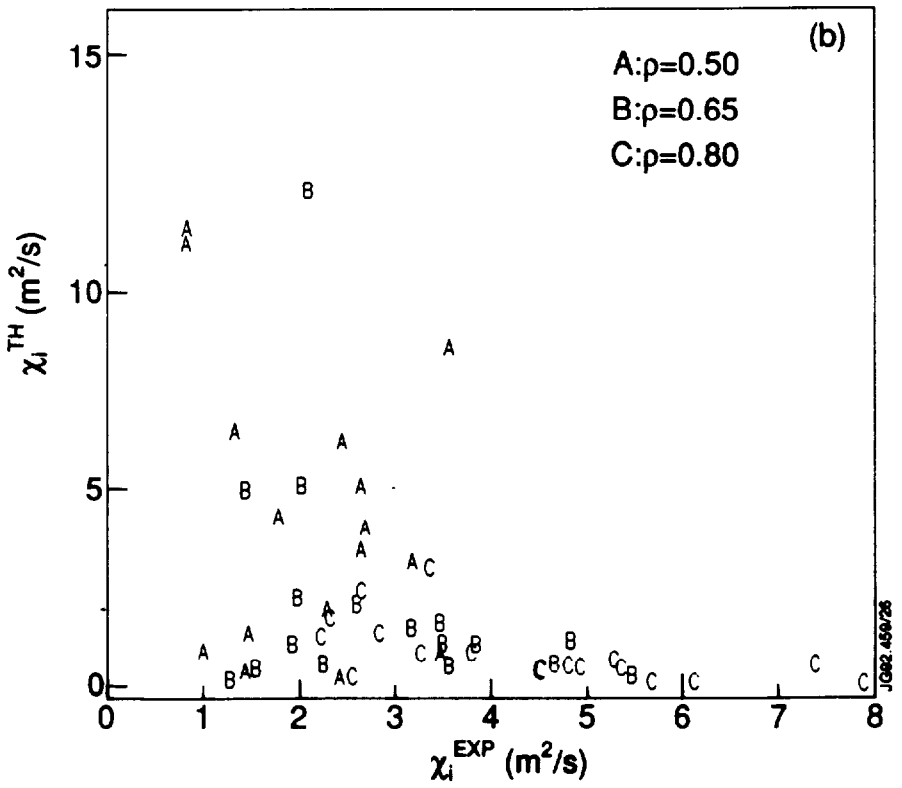

b) the region with $q > 1$ of plasmas for which χ_i can be inferred from the experimental data with uncertainty $< \pm 50\%$.

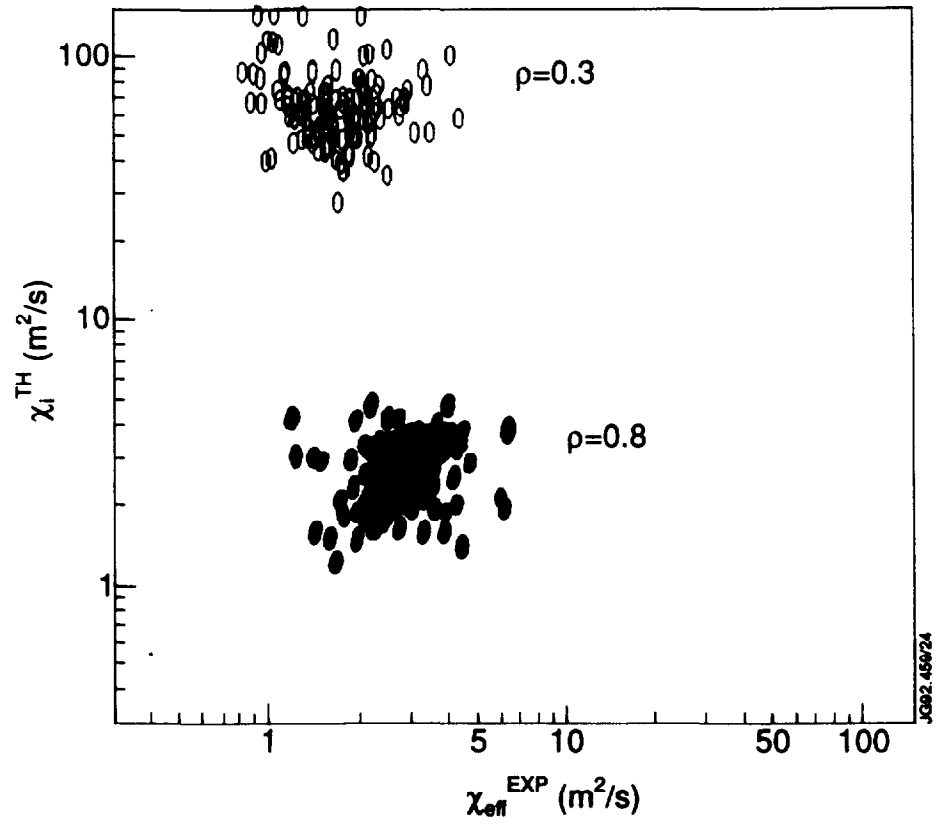

Figure 18

Comparison of the theoretical ion thermal conductivity of Biglari et al. Eq.(24), under the assumption of long wavelength modes, with the measured "effective" transport coefficient at two radial positions for JET sawtooth-free plasmas.

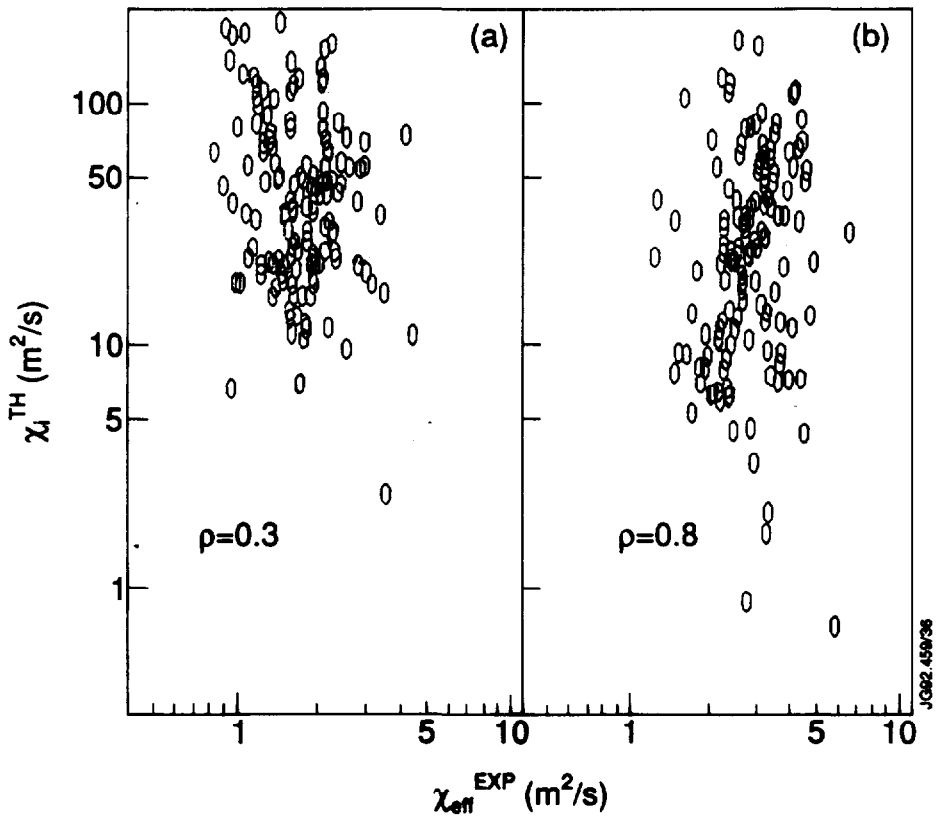

Figure 19

Comparison of the theoretical ion thermal conductivity of Xu and Rosenbluth Eq.(30) with the measured "effective" transport coefficient at two radial positions for JET sawtooth-free plasmas.

Figure 20

Comparison of the ion thermal conductivity of Xu and Rosenbluth for the magnetic trapped ion mode Eq.(36) with the transport coefficient inferred from the measurements for:

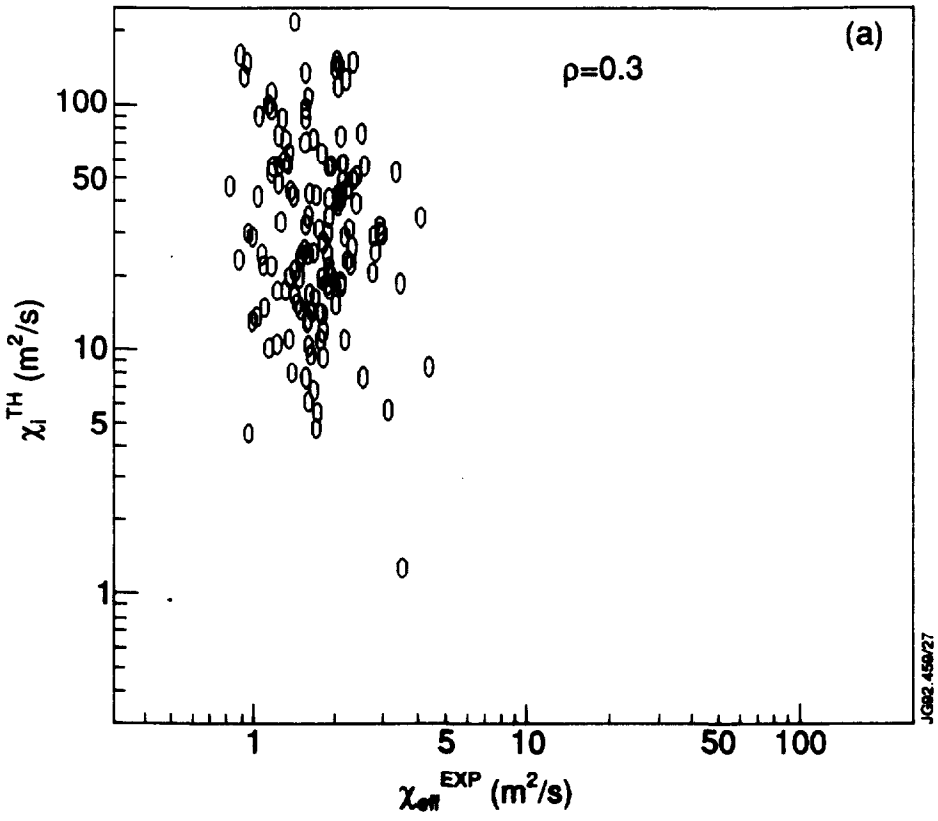

a) the core plasma region of sawtooth-free discharges (same data set as in Figure 4);

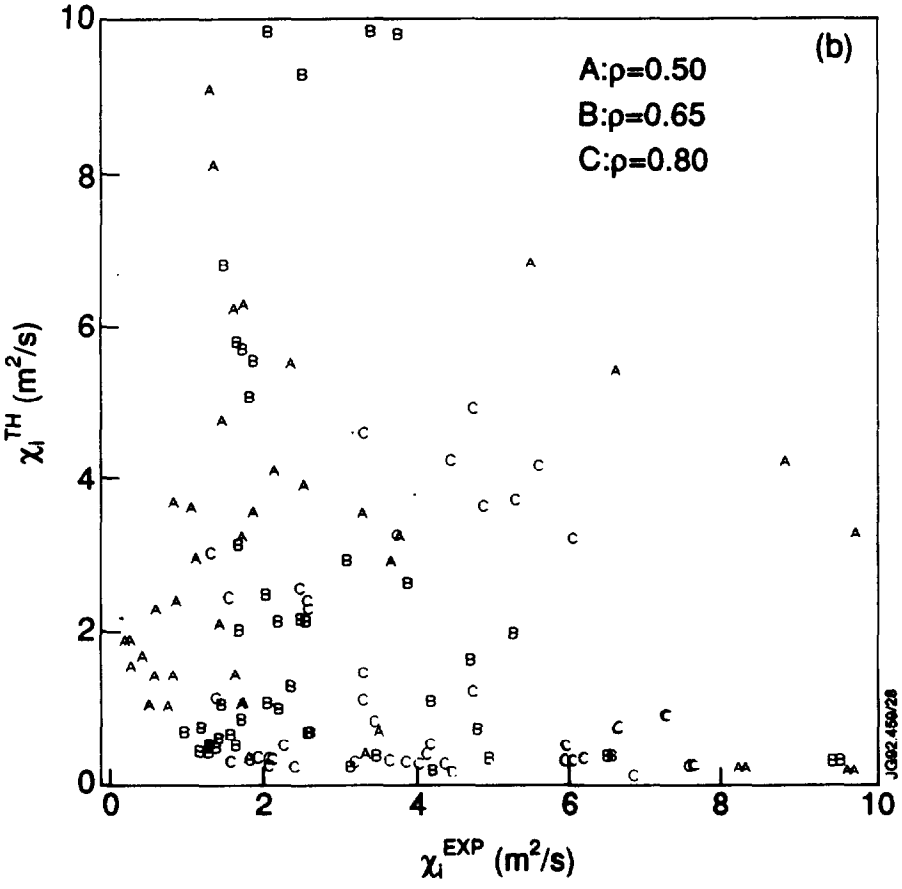

b) the region $q > 1$ of plasmas for which a reliable estimate of the experimental χ_i is available.

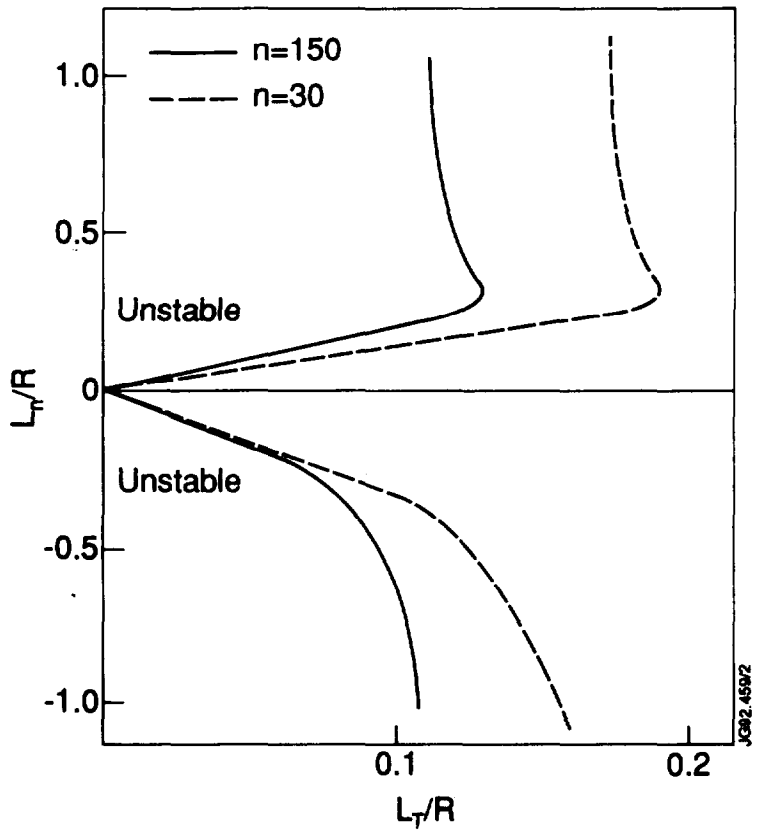

Figure 21

Stability boundaries for the trapped ion mode in the $(\varepsilon_n, \varepsilon_T)$ plane as obtained by Garbet et al. [31] for two different values of the toroidal mode number.

Appendix I

THE JET TEAM

JET Joint Undertaking, Abingdon, Oxon, OX14 3EA, U.K.

J.M. Adams[1], B. Alper, H. Altmann, A. Andersen[14], P. Andrew, S.Ali-Arshad, W. Bailey, B. Balet, P. Barabaschi, Y. Baranov, P. Barker, R. Barnsley[2], M. Baronian, D.V. Bartlett, A.C. Bell, G. Benali, P. Bertoldi, E. Bertolini, V. Bhatnagar, A.J. Bickley, D. Bond, T. Bonicelli, S.J. Booth, G. Bosia, M. Botman, D. Boucher, P. Boucquey, M. Brandon, P. Breger, H. Brelen, W.J. Brewerton, H. Brinkschulte, T. Brown, M. Brusati, T. Budd, M. Bures, P. Burton, T. Businaro, P. Butcher, H. Buttgereit, C. Caldwell-Nichols, D.J. Campbell, D. Campling, P. Card, G. Celentano, C.D. Challis, A.V.Chankin[23], A. Cherubini, D. Chiron, J. Christiansen, P. Chuilon, R. Claesen, S. Clement, E. Clipsham, J.P. Coad, I.H. Coffey[24], A. Colton, M. Comiskey[4], S. Conroy, M. Cooke, S. Cooper, J.G. Cordey, W. Core, G. Corrigan, S. Corti, A.E. Costley, G. Cottrell, M. Cox[7], P. Crawley, O. Da Costa, N. Davies, S.J. Davies[7], H. de Blank, H. de Esch, L. de Kock, E. Deksnis, N. Deliyanakus, G.B. Denne-Hinnov, G. Deschamps, W.J. Dickson[19], K.J. Dietz, A. Dines, S.L. Dmitrenko, M. Dmitrieva[25], J. Dobbing, N. Dolgetta, S.E. Dorling, P.G. Doyle, D.F. Düchs, H. Duquenoy, A. Edwards, J. Ehrenberg, A. Ekedahl, T. Elevant[11], S.K. Erents[7], L.G. Eriksson, H. Fajemirokun[12], H. Falter, J. Freiling[15], C. Froger, P. Froissard, K. Fullard, M. Gadeberg, A. Galetsas, L. Galbiati, D. Gambier, M. Garribba, P. Gaze, R. Giannella, A. Gibson, R.D. Gill, A. Girard, A. Gondhalekar, D. Goodall[7], C. Gormezano, N.A. Gottardi, C. Gowers, B.J. Green, R. Haange, A. Haigh, C.J. Hancock, P.J. Harbour, N.C. Hawkes[7], N.P. Hawkes[1], P. Haynes[7], J.L. Hemmerich, T. Hender[7], J. Hoekzema, L. Horton, J. How, P.J. Howarth[5], M. Huart, T.P. Hughes[4], M. Huguet, F. Hurd, K. Ida[18], B. Ingram, M. Irving, J. Jacquinot, H. Jaeckel, J.F. Jaeger, G. Janeschitz, Z. Jankowicz[22], O.N. Jarvis, F. Jensen, E.M. Jones, L.P.D.F. Jones, T.T.C. Jones, J-F. Junger, F. Junique, A. Kaye, B.E. Keen, M. Keilhacker, W. Kerner, N.J. Kidd, R. Konig, A. Konstantellos, P. Kupschus, R. Lässer, J.R. Last, B. Laundy, L. Lauro-Taroni, K. Lawson[7], M. Lennholm, J.Lingertat[13], R.N. Litunovski, A. Loarte, R. Lobel, P. Lomas, M. Loughlin, C. Lowry, A.C. Maas[15], B. Macklin, C.F. Maggi[16], G. Magyar, V. Marchese, F. Marcus, J. Mart, D. Martin, E. Martin, R. Martin-Solis[8], P. Massmann, G. Matthews, H. McBryan, G. McCracken[7], P. Meriguet, P. Miele, S.F. Mills, P. Millward, E. Minardi[16], R. Mohanti[17], P.L. Mondino, A. Montvai[3], P. Morgan, H. Morsi, G. Murphy, F. Nave[27], S. Neudatchin[23], G. Newbert, M. Newman, P. Nielsen, P. Noll, W. Obert, D. O'Brien, J. O'Rourke, R. Ostrom, M. Ottaviani, S. Papastergiou, D. Pasini, B. Patel, A. Peacock, N. Peacock[7], R.J.M. Pearce, D. Pearson[12], J.F. Peng[26], R. Pepe de Silva, G. Perinic, C. Perry, M.A. Pick, J. Plancoulaine, J-P. Poffé, R. Pohlchen, F. Porcelli, L. Porte[19], R. Prentice, S. Puppin, S. Putvinskii[23], G. Radford[9], T. Raimondi, M.C. Ramos de Andrade, M. Rapisarda[29], P-H. Rebut, R. Reichle, S. Richards, E. Righi, F. Rimini, A. Rolfe, R.T. Ross, L. Rossi, R. Russ, H.C. Sack, G. Sadler, G. Saibene, J.L. Salanave, G. Sanazzaro, A. Santagiustina, R. Sartori, C. Sborchia, P. Schild, M. Schmid, G. Schmidt[6], H. Schroepf, B. Schunke, S.M. Scott, A. Sibley, R. Simonini, A.C.C. Sips, P. Smeulders, R. Smith, M. Stamp, P. Stangeby[20], D.F. Start, C.A. Steed, D. Stork, P.E. Stott, P. Stubberfield, D. Summers, H. Summers[19], L. Svensson, J.A. Tagle[21], A. Tanga, A. Taroni, C. Terella, A. Tesini, P.R. Thomas, E. Thompson, K. Thomsen, P. Trevalion, B. Tubbing, F. Tibone, H. van der Beken, G. Vlases, M. von Hellermann, T. Wade, C. Walker, D. Ward, M.L. Watkins, M.J. Watson, S. Weber[10], J. Wesson, T.J. Wijnands, J. Wilks, D. Wilson, T. Winkel, R. Wolf, D. Wong, C. Woodward, M. Wykes, I.D. Young, L. Zannelli, A. Zolfaghari[28], G. Zullo, W. Zwingmann.

PERMANENT ADDRESSES

1. UKAEA, Harwell, Didcot, Oxon, UK.
2. University of Leicester, Leicester, UK.
3. Central Research Institute for Physics, Budapest, Hungary.
4. University of Essex, Colchester, UK.
5. University of Birmingham, Birmingham, UK.
6. Princeton Plasma Physics Laboratory, New Jersey, USA.
7. UKAEA Culham Laboratory, Abingdon, Oxon, UK.
8. Universidad Complutense de Madrid, Spain.
9. Institute of Mathematics, University of Oxford, UK.
10. Freien Universität, Berlin, F.R.G.
11. Royal Institute of Technology, Stockholm, Sweden.
12. Imperial College, University of London, UK.
13. Max Planck Institut für Plasmaphysik, Garching, FRG.
14. Risø National Laboratory, Denmark.
15. FOM Instituut voor Plasmafysica, Nieuwegein, The Netherlands.
16. Dipartimento di Fisica, University of Milan, Milano, Italy.
17. North Carolina State University, Raleigh, NC, USA
18. National Institute for Fusion Science, Nagoya, Japan.
19. University of Strathclyde, 107 Rottenrow, Glasgow, UK.
20. Institute for Aerospace Studies, University of Toronto, Ontario, Canada.
21. CIEMAT, Madrid, Spain.
22. Institute for Nuclear Studies, Otwock-Swierk, Poland.
23. Kurchatov Institute of Atomic Energy, Moscow, USSR
24. Queens University, Belfast, UK.
25. Keldysh Institute of Applied Mathematics, Moscow, USSR.
26. Institute of Plasma Physics, Academica Sinica, Hefei, P. R. China.
27. LNETI, Savacem, Portugal.
28. Plasma Fusion Center, M.I.T., Boston, USA.
29. ENEA, Frascati, Italy.

At 1st July, 1992